J. Fluid Mech. (1997), *vol.* 339, *pp.* 357–390. Printed in the United Kingdom

Large-eddy simulation of the turbulent mixing layer

By BERT VREMAN, BERNARD GEURTS AND HANS KUERTEN

Department of Applied Mathematics, University of Twente, PO Box 217, 7500 AE Enschede, The Netherlands
e-mail: vreman@math.utwente.nl

(Received 23 November 1995 and in revised form 23 January 1997)

Six subgrid models for the turbulent stress tensor are tested by conducting large-eddy simulations (LES) of the weakly compressible temporal mixing layer: the Smagorinsky, similarity, gradient, dynamic eddy-viscosity, dynamic mixed and dynamic Clark models. The last three models are variations of the first three models using the dynamic approach. Two sets of simulations are performed in order to assess the quality of the six models. The LES results corresponding to the first set are compared with filtered results obtained from a direct numerical simulation (DNS). It appears that the dynamic models lead to more accurate results than the non-dynamic models tested. An adequate mechanism to dissipate energy from resolved to subgrid scales is essential. The dynamic models have this property, but the Smagorinsky model is too dissipative during transition, whereas the similarity and gradient models are not sufficiently dissipative for the smallest resolved scales. In this set of simulations, at moderate Reynolds number, the dynamic mixed and Clark models are found to be slightly more accurate than the dynamic eddy-viscosity model. The second set of LES concerns the mixing layer at a considerably higher Reynolds number and in a larger computational domain. An accurate DNS for this mixing layer can currently not be performed, thus in this case the LES are tested by investigating whether they resemble a self-similar turbulent flow. It is found that the dynamic models generate better results than the non-dynamic models. The closest approximation to a self-similar state was obtained using the dynamic eddy-viscosity model.

1. Introduction

Large-eddy simulation (LES) is an important technique to simulate turbulent flows. In LES the large-scale motions in the flow are solved, whereas the effect of the small-scale motions is modelled by a so-called subgrid model (Rogallo & Moin 1984). LES requires less computational effort or can simulate flows at higher Reynolds numbers than direct numerical simulation (DNS), which attempts to solve all scales present in the turbulent flow. The turbulent stress tensor τ_{ij} is the most important subgrid term in LES. Much effort has been put into the development of good subgrid models for this tensor (Moin & Jimenez 1993) and, consequently, a large number of subgrid models exist. The purpose of this paper is to perform a comparative study of LES using various subgrid models. We do not focus on numerical methods, but systematically investigate and compare the characteristic behaviour of a number of subgrid models in actual LES of a free shear flow.

The flow simulated is the three-dimensional temporal compressible mixing layer. Direct numerical simulations of the turbulent mixing layer at various Mach numbers have been reported in literature. We mention the incompressible simulations by Comte, Lesieur & Lamballais (1992) and Rogers & Moser (1993) and the highly compressible simulations at convective Mach numbers 0.8 and 1.2 (Luo & Sandham 1994 and Vreman, Sandham & Luo 1996*c*, respectively). The mixing layer in this paper is simulated at a low convective Mach number of 0.2. At this Mach number the physical characteristics of the flow are similar to those of the incompressible flow (Sandham & Reynolds 1991). Furthermore, the subgrid modelling in LES of this flow can be regarded as incompressible. This implies that the turbulent stress tensor is the only subgrid term which needs to be modelled (Vreman 1995).

In this paper we test the following subgrid models for the turbulent stress tensor: the Smagorinsky model (Smagorinsky 1963), the similarity model (Bardina, Ferziger & Reynolds 1984; Liu, Meneveau & Katz 1994*a*), the gradient model (Clark, Ferziger & Reynolds 1979; Liu *et al.* 1994*a*), the dynamic eddy-viscosity model (Germano 1992), the dynamic mixed model (Zang, Street & Koseff 1993; Vreman, Geurts & Kuerten 1994*b*) and the dynamic Clark model (Vreman, Geurts & Kuerten 1996*b*). Among these models are important representatives of the available subgrid models. Three models employ the dynamic procedure (Germano 1992) in order to adjust the value of the model coefficient to the local turbulence. We have restricted this study to models which do not require the solution of an additional differential equation (Ghosal *et al.* 1995).

Two sets of LES are conducted to test these subgrid-models. The tests are so-called *a posteriori* tests, to be distinguished from *a priori* tests in which no LES are performed (Meneveau 1994; Vreman, Geurts & Kuerten 1995). The LES results in the first set are compared with filtered DNS results. The Reynolds number in this case (specified in §3.1) is low, which is required to perform an accurate DNS with the present computer capacity. The simulations in the second set are performed at a higher Reynolds number and in a larger computational domain than in the first set. These results are not compared with DNS data (DNS for this flow would require too much computational effort), but are judged with respect to the degree of self-similarity.

Although the flow considered in this paper is not physically realizable due to the periodic boundary condition in the streamwise direction, it displays many characteristic features of turbulence, like the energy cascade and inertial subrange, which are main elements to be captured in subgrid modelling. A detailed quantitative comparison between model predictions and experimental findings is not possible due to the temporal framework of the simulation. However, a qualitative comparison of the dominant mechanisms can be made. Based on the present study we arrive at the identification and explanation of shortcomings of subgrid models, which provides a basis for future modelling of more complex, spatially evolving, flows.

The paper is organized as follows. The mathematical formulation, specifying governing equations, numerical approach and subgrid models, is found in §2. The comparison of LES results with filtered DNS data is subject of §3. In §4 results from the second set of simulations are presented. Section 5 summarizes the conclusions. In the Appendix the effective filter width of the filter resulting from two consecutively applied top-hat filters is estimated, which is needed in the dynamic procedure.

2. Mathematical formulation

In the first subsection we will describe the configuration of the mixing layer, the filtered Navier–Stokes equations and the numerical discretization. The subgrid models will be formulated in the second subsection.

2.1. *Governing equations*

The temporal mixing layers simulated contain two streams with equal and opposite free-stream speed U, which is used as reference velocity. Other reference values are half the initial vorticity thickness (L_R) and the free-stream values for the density (ρ_R), temperature (T_R) and viscosity (μ_R). The free-stream Mach number M (also the convective Mach number in this case) equals 0.2. The mixing layers are solved in a cubic domain $[0, L] \times [-\frac{1}{2}L, \frac{1}{2}L] \times [0, L]$, where the streamwise, normal and spanwise directions are denoted by x_1, x_2 and x_3 respectively. Periodic boundary conditions are imposed in the stream- and spanwise directions, whereas the boundaries in the normal direction are free-slip walls. The non-dimensionalized initial mean velocity profile is given by $u_1 = \tanh(x_2)$, whereas the initial temperature profile is obtained from the Crocco–Busemann law (Ragab & Wu 1989) and the initial mean pressure distribution is uniform. In order to initiate turbulence, either a random or an eigenfunction perturbation is superimposed on the mean profile.

The mixing layer is simulated in a compressible framework, because the work reported here is part of a research project on compressible flow. The interesting compressibility effects in this flow are discussed elsewhere (Vreman *et al.* 1996*c*).

The partial differential equations which govern a compressible flow are the Navier–Stokes equations, representing conservation of mass, momentum and energy. In DNS these equations are directly solved, but in the LES approach these equations are filtered in order to reduce the number of scales to be solved. The filter operation extracts the large-scale part $\bar{f}$ from a flow variable f. In this paper we employ the top-hat filter (Vreman, Geurts & Kuerten 1994*a*) with filter width Δ, representing the size of the smallest eddies resolved in LES. For compressible flows, Favre (1983) introduced a related filter operation, $\tilde{f} = \overline{\rho f}/\bar{\rho}$, where ρ denotes the fluid density.

The filtered Navier–Stokes equations can be written in the following form (Vreman 1995):

$$\partial_t \bar{\rho} + \partial_j(\bar{\rho}\tilde{u}_j) = 0, \tag{2.1}$$

$$\partial_t(\bar{\rho}\tilde{u}_i) + \partial_j(\bar{\rho}\tilde{u}_i\tilde{u}_j) + \partial_i\bar{p} - \partial_j\check{\sigma}_{ij} = -\partial_j(\bar{\rho}\tau_{ij}) + R_i, \tag{2.2}$$

$$\partial_t\check{e} + \partial_j((\check{e} + \bar{p})\tilde{u}_j) - \partial_j(\check{\sigma}_{ij}\tilde{u}_i) + \partial_j\check{q}_j = R_e, \tag{2.3}$$

where t represents time and the symbols ∂_t and ∂_j denote the partial differential operators $\partial/\partial t$ and $\partial/\partial x_j$ respectively. Furthermore, the summation convention for repeated indices is used.

Concerning the flow variables, the Favre-filtered velocity vector is denoted by $\tilde{\boldsymbol{u}}$, while $\bar{\rho}$ is the filtered density and $\bar{p}$ the filtered pressure; $\check{e}$ is the total energy density of the filtered variables $\check{e} = \bar{p}/(\gamma - 1) + \frac{1}{2}\bar{\rho}\tilde{u}_i\tilde{u}_i$. The filtered temperature $\tilde{T}$ is related to the filtered density and pressure by the ideal gas law, $\bar{\rho}\tilde{T} = \gamma M^2\bar{p}$ in non-dimensional form. The ratio of the specific heats C_V and C_P is denoted by γ and is given the value 1.4.

The viscous stress tensor based on filtered variables is defined as $\check{\sigma}_{ij} = (\tilde{\mu}/Re)\tilde{S}_{ij}$. The viscosity $\tilde{\mu}(= \mu(\tilde{T}))$ is calculated from Sutherland's law for air, Re is the Reynolds

number based on the reference values introduced above, and

$$\tilde{S}_{ij} = \partial_j \tilde{u}_i + \partial_i \tilde{u}_j - \tfrac{2}{3}\delta_{ij}\partial_k \tilde{u}_k, \tag{2.4}$$

is the strain rate based on the Favre-filtered velocity, where δ_{ij} is the Kronecker delta. The symbol $\breve{\boldsymbol{q}}$ in the energy equation represents the heat flux vector proportional to the gradient of the filtered temperature, where the Prandtl number equals 1.

In this description the left-hand sides of (2.1)–(2.3) are the Navier–Stokes equations expressed in the filtered variables $\bar{\rho}$, $\tilde{u}_j$ and $\bar{p}$. The right-hand sides of the filtered equations are the so-called subgrid terms. The most important subgrid-term occurs in the momentum equation (2.2) and contains the turbulent stress tensor, defined as

$$\tau_{ij} = \widetilde{u_i u_j} - \tilde{u}_i \tilde{u}_j. \tag{2.5}$$

The subgrid term R_i, resulting from the nonlinearity in the viscous stress tensor, and the subgrid terms in the energy equation (2.3), denoted by R_e, can be neglected for this flow and this Mach number (Vreman 1995).

The Navier–Stokes equations (in DNS) and filtered Navier–Stokes equations (in LES) are discretized using central differences on a non-staggered uniform grid with grid spacing h. The time integration is explicit and is performed with a compact-storage second-order accurate four-stage Runge–Kutta method (Vreman 1995). The convective terms (including pressure) are discretized with a robust fourth-order method, which approximates e.g. $\partial_1 f$ as (Vreman, Geurts & Kuerten 1996*a*)

$$(\partial_1 f)_{i,j,k} \approx (-s_{i+2,j,k} + 8s_{i+1,j,k} - 8s_{i-1,j,k} + s_{i-2,j,k})/(12h_1) \tag{2.6}$$

with $$s_{i,j,k} = (-g_{i,j-2,k} + 4g_{i,j-1,k} + 10g_{i,j,k} + 4g_{i,j+1,k} - g_{i,j+2,k})/16,$$

with $$g_{i,j,k} = (-f_{i,j,k-2} + 4f_{i,j,k-1} + 10f_{i,j,k} + 4f_{i,j,k+1} - f_{i,j,k+2})/16.$$

The viscous terms contain second-order derivatives and are calculated with second-order accuracy. The viscous stress tensor, the turbulent stress tensor in LES and the heat flux are calculated in centres of cells. In centre $(i+\frac{1}{2}, j+\frac{1}{2}, k+\frac{1}{2})$ the derivative $\partial_1 f$ is approximated as

$$(\partial_1 f)_{i+\frac{1}{2},j+\frac{1}{2},k+\frac{1}{2}} \approx (s_{i+1,j+\frac{1}{2},k+\frac{1}{2}} - s_{i,j+\frac{1}{2},k+\frac{1}{2}})/h \tag{2.7}$$

with $$s_{i,j+\frac{1}{2},k+\frac{1}{2}} = (f_{i,j,k} + f_{i,j+1,k} + f_{i,j,k+1} + f_{i,j+1,k+1})/4.$$

The divergences of the viscous stress tensor and heat flux are subsequently calculated with the same discretization rule applied to control volumes centred around vertices (i, j, k).

It is important that the dissipation caused by the numerical scheme is small. For this reason Blaisdell, Mansour & Reynolds (1993) recast the convective terms in the compressible momentum equation in the skew-symmetric form (see Gresho 1991 for an overview of the existing forms for incompressible flow). A central scheme applied to the skew-symmetric form is 'kinetic energy-conserving', i.e. the total kinetic energy is conserved apart from viscous and compressibility effects, but loses the conservation of momentum. Although this scheme prevents a 'blow up' of kinetic energy, it does not guarantee that other possible instabilities in a compressible solver will not occur (e.g. locally negative temperature) (see §4). Our scheme discretizes the convective terms in their standard divergence form and, consequently, mass, momentum and total energy (kinetic plus internal energy) are conserved. We will verify that the numerical dissipation of the scheme is small, albeit not zero (see §3.2.2). For the same reason we do not use any explicit artificial dissipation. If the spatial resolution

	Model for τ_{ij}	Curve
M0	0 (no model)	solid
M1	Smagorinsky	*
M2	similarity	×
M3	gradient	+
M4	dynamic eddy viscosity	dashed
M5	dynamic mixed	dotted
M6	dynamic Clark	dashed-dotted

TABLE 1. Subgrid models for the turbulent stress tensor.

is sufficient, the dissipation provided by the viscous and subgrid terms makes the numerical method stable.

The filter width Δ in LES is set equal to $2h$, indicating that a minimum of two grid points is taken to represent the smallest eddies resolved in LES. Compared to $\Delta = h$, LES results obtained with $\Delta = 2h$ are less sensitive to discretization errors. In several studies it was found that $\Delta = 2h$ leads to more accurate results than $\Delta = h$ (Kwak, Reynolds & Ferziger 1975; Vreman *et al.* 1996*a*) and in some cases even $\Delta/h > 2$ seems necessary (Lund, Kaltenback & Akselvdl 1995). A larger Δ/h ratio leads to smaller discretization errors, but on the other hand the Δ/h ratio is required to be as small as possible in order to retain a maximum amount of information in the resolved scales. An explicit use of the filter is only made in some of the subgrid models and in filtering the DNS data.

2.2. *Subgrid models*

In total six models for the turbulent stress tensor τ_{ij} as it appears in the subgrid term in the momentum equation will be investigated in this paper. For transparency we present the incompressible formulations in which $\rho = 1$. In this case the Favre filter reduces to the 'bar' filter and the turbulent stress tensor is written as

$$\tau_{ij} = \overline{u_i u_j} - \overline{u}_i \overline{u}_j. \tag{2.8}$$

The compressible formulations of the subgrid models are given in Vreman (1995).

The names of the models for τ_{ij} with their abbreviations used here are listed in table 1. We consider three non-dynamic subgrid models (M1–3) and three dynamic subgrid models (M4–6). The first three models form the basis of the latter three. M4 is the dynamic version of the Smagorinsky model (M1), whereas in M5 the similarity model (M2) and in M6 the gradient model (M3) are supplemented with a dynamic eddy viscosity. The abbreviation M0 corresponds to the case in which τ_{ij} is simply omitted. In this case the LES is in fact a DNS on the coarse LES grid starting from filtered initial conditions. The case M0 is included in order to provide a point of reference for the other subgrid models.

2.2.1. *The Smagorinsky model*

The first model is the well-known Smagorinsky model (M1) (Smagorinsky 1963; Rogallo & Moin 1984), given by

$$\tau_{ij}^{(1)} = -C_S^2 \Delta^2 |\overline{S}| \overline{S}_{ij} \quad \text{with} \quad |\overline{S}|^2 = \tfrac{1}{2}\overline{S}_{ij}^2. \tag{2.9}$$

Several values have been proposed for the Smagorinsky constant C_S: e.g. 0.2 in isotropic turbulence (Deardorff 1971) and 0.1 in turbulent channel flow (Deardorff

1970). With the use of power laws for the shape of the energy spectrum, Schumann (1991) suggests $C_S = 0.17$. In this paper we use the latter value 0.17 and discuss the effect of adopting a lower value in §4. The Smagorinsky model is often too dissipative in laminar regions with mean shear (Germano *et al.* 1991) and the correlation with the actual turbulent stress tensor is usually quite low (about 0.3 in several flows). The similarity and gradient model, described below, are less dissipative in laminar regimes and correlate much better with the actual turbulent stress (0.6 to 0.9 in several flows (Liu *et al.* 1994*a*; Vreman *et al.* 1995)).

2.2.2. *The similarity model*

The similarity model (M2), formulated by Bardina *et al.* (1984) and revisited by Liu *et al.* (1994*a*), is not of the eddy-viscosity type. It is based on the assumption that the velocities at different levels give rise to turbulent stresses with similar structures. More specifically, the definition of τ_{ij} in terms of the unfiltered variables u_i is applied to the filtered variables $\overline{u}_i$:

$$\tau_{ij}^{(2)} = \overline{\overline{u}_i \overline{u}_j} - \overline{\overline{u}}_i \overline{\overline{u}}_j. \tag{2.10}$$

In contrast to eddy-viscosity models, this model has a mechanism to represent backscatter of energy from subgrid to resolved scales.

2.2.3. *The gradient model*

The gradient model (M3) expresses τ_{ij} as an inner product of velocity gradients (Clark *et al.* 1979; Liu *et al.* 1994*a*):

$$\tau_{ij}^{(3)} = \tfrac{1}{12} \Delta^2 (\partial_k \overline{u}_i)(\partial_k \overline{u}_j). \tag{2.11}$$

This model is equal to the lowest-order term in Δ after substituting the following Taylor expansions into the similarity model (2.10):

$$\overline{\overline{u}_i \overline{u}_j} = \overline{u}_i \overline{u}_j + \tfrac{1}{24} \Delta^2 \partial_{kk} (\overline{u}_i \overline{u}_j) + O(\Delta^4), \tag{2.12}$$

$$\overline{\overline{u}}_i = \overline{u}_i + \tfrac{1}{24} \Delta^2 \partial_{kk} \overline{u}_i + O(\Delta^4). \tag{2.13}$$

To obtain the gradient model we expanded the similarity model and not the real turbulent stress τ_{ij} itself. An expansion of τ_{ij} itself involves Taylor series expansions of the rapidly fluctuating *unfiltered* velocity field (Rogallo & Moin 1984). An expansion of the similarity model is more appropriate since it involves Taylor series expansions of *filtered* quantities only, which are varying much more smoothly over a length of order Δ than unfiltered quantities. A reason to consider the gradient model is its higher efficiency in actual simulations when compared to the similarity model. No extra filterings are needed and the derivatives of the velocity can be reused in the calculation of the viscous stresses.

Simulations with the pure gradient model (2.11) appear to be unstable (Vreman, Geurts & Kuerten 1996*b*). Clark *et al.* (1979) added the Smagorinsky model, but the resulting model inherits the excessive dissipation of the Smagorinsky model. We follow another approach, suggested by Liu *et al.* (1994*a*) and supply the gradient model with a 'limiter' to prevent energy backscatter. In this procedure the subgrid model is prescribed by $c\tau_{ij}^{(3)}$, i.e. the gradient model multiplied with a function c. The function c equals one if $\tau_{ij}^{(3)} \partial_j \overline{u}_i \leqslant 0$ and zero otherwise. This substitution ensures that the subgrid model dissipates energy from resolved to subgrid scales.

2.2.4. *The dynamic eddy-viscosity model*

The excessive dissipation of the Smagorinsky model in laminar regimes is overcome if the model constant is replaced by a coefficient which is dynamically obtained and depends on the local structure of the flow. Such a dynamic eddy-viscosity model (M4), which has been proposed by Germano (1992), has successfully been applied to a number of flows (Moin & Jimenez 1993). This model adopts Smagorinsky's eddy-viscosity formulation, but the square of the Smagorinsky constant C_S is replaced by a coefficient C_d:

$$\tau_{ij}^{(4)} = -C_d \Delta^2 |\overline{S}| \overline{S}_{ij}. \tag{2.14}$$

The coefficient C_d is dynamically adjusted to the local structure of the flow using the following procedure. First, apart from the basic filter level (F-level), denoted by the bar filter, Germano introduced a test filter (at the G-level), which is denoted by a hat ($\hat{.}$) and corresponds to a filter width 2Δ. The consecutive application of these two filters, resulting in e.g. $\widehat{\overline{u}_i}$, defines a filter on the 'FG-level' with which a filter width $\kappa\Delta$ can be associated. For top-hat filters, adopted in this work, the optimum value for κ equals $\sqrt{5}$ (see the Appendix). Next we consider Germano's identity, which reads

$$T_{ij} - \hat{\tau}_{ij} = L_{ij}. \tag{2.15}$$

The right-hand side of (2.15) can explicitly be calculated from the variables on the F-level:

$$L_{ij} = \widehat{\overline{u}_i \overline{u}_j} - \hat{\overline{u}}_i \hat{\overline{u}}_j, \tag{2.16}$$

The terms on the left-hand side of the Germano identity are the turbulent stress on the FG-level,

$$T_{ij} = \widehat{\overline{u_i u_j}} - \hat{\overline{u}}_i \hat{\overline{u}}_j, \tag{2.17}$$

and the turbulent stress on the F-level filtered with the test filter, respectively. The terms on the left-hand side cannot be calculated from the variables on the F-level.

The subgrid model (equation (2.14)) is substituted into the Germano identity, which means that expressions for T_{ij} and τ_{ij} are obtained by formulating the subgrid model in FG-filtered quantities and F-filtered quantities, respectively. This yields

$$C_d M_{ij} = L_{ij}, \tag{2.18}$$

with

$$M_{ij} = -(\kappa\Delta)^2 |\hat{\overline{S}}| \hat{\overline{S}}_{ij} + \Delta^2 \widehat{|\overline{S}| \overline{S}_{ij}}. \tag{2.19}$$

Since equation (2.18) represents a system of equations for the single unknown C_d, a least-squares approach (Lilly 1992) is followed to calculate the model coefficient,

$$C_d = \frac{\langle M_{ij} L_{ij} \rangle}{\langle M_{ij} M_{ij} \rangle}. \tag{2.20}$$

In order to prevent numerical instability caused by negative values of C_d, the numerator and denominator in equation (2.20) are averaged over the homogeneous directions, which is expressed by the symbol $\langle . \rangle$. Furthermore, the model coefficient C_d is artificially set to zero at locations where the right-hand side of (2.20) has negative values. One assumption of the formulation above is that variations of C_d on the scale of the test filter are small. An alternative formulation which does not require this assumption has been proposed by Piomelli & Liu (1994). Some LES in this paper have been repeated using this formulation, but no significant differences were found.

2.2.5. *The dynamic mixed model*

The relatively accurate representation of the turbulent stress by the similarity model and a proper dissipation provided by the dynamic eddy-viscosity concept are combined in the dynamic mixed model (Zang *et al.* 1993; Vreman *et al.* 1994*b*). The dynamic mixed model (M5) employs the sum of the similarity and Smagorinsky eddy-viscosity model as base model:

$$\overline{\rho}\tau_{ij}^{(5)} = \overline{\rho}\tau_{ij}^{(2)} - C_d\Delta^2|\overline{S}|\overline{S}_{ij}. \tag{2.21}$$

The dynamic model coefficient C_d is obtained by substitution of this model into the Germano identity, which yields

$$H_{ij} + C_d M_{ij} = L_{ij}, \tag{2.22}$$

where the tensors L_{ij} and M_{ij} are defined by equations (2.16) and (2.19) and the tensor H_{ij} is defined as

$$H_{ij} = \widehat{\widehat{\overline{u}_i}\widehat{\overline{u}_j}} - \widehat{\overline{u}}_i\widehat{\overline{u}}_j - (\widehat{\overline{u}_i\overline{u}_j} - \widehat{\overline{u}}_i\widehat{\overline{u}}_j). \tag{2.23}$$

By analogy with the formulation of the dynamic eddy-viscosity model, the dynamic model coefficient is obtained with the least-squares approach:

$$C_d = \frac{\langle M_{ij}(L_{ij} - H_{ij})\rangle}{\langle M_{ij}M_{ij}\rangle}, \tag{2.24}$$

which completes the formulation of the dynamic mixed model.

2.2.6. *The dynamic Clark model*

Finally, we consider the dynamic Clark model (M6) (Vreman *et al.* 1996*b*), which employs the Clark model as base model:

$$\tau_{ij}^{(6)} = \tau_{ij}^{(3)} - C_d\Delta^2|\overline{S}|\overline{S}_{ij}. \tag{2.25}$$

The formulation is similar to the formulation of M5, the only difference being the 'gradient' part M3, which replaces the similarity part M2 of the model M5. Substitution of the dynamic Clark model into the Germano identity yields equation (2.22) for C_d. In this case the tensor H_{ij} expresses the difference of the gradient model on the FG-level and the F-level:

$$H_{ij} = \tfrac{1}{12}(\kappa\Delta_k)^2\partial_k\widehat{\overline{u}}_i\partial_k\widehat{\overline{u}}_j - \tfrac{1}{12}\Delta_k^2\partial_k\widehat{\overline{u}_i\partial_k\overline{u}}_j. \tag{2.26}$$

The dynamic model coefficient C_d is obtained from the right-hand side of expression (2.24). Unlike the gradient model M3, the model M6 does not require a limiter for stability purposes. Model M6 requires less computational effort than the dynamic mixed model, in the same way that M3 is cheaper than M2.

3. Agreement with filtered DNS data

In this section the performance of the six subgrid models is tested in actual LES and the results are compared with filtered DNS results.

3.1. *Description of DNS and LES*

We simulate the three-dimensional temporal mixing layer described in §2.1. The length L of the domain is set equal to four times the wavelength of the most unstable mode according to linear stability theory, thus allowing two subsequent pairings of

spanwise rollers. The initial condition is formed by the mean profiles superimposed with two- and three-dimensional perturbation modes obtained from linear stability theory (Sandham & Reynolds 1991). A single mode is denoted with (α, β), where α is the streamwise and β the spanwise wavenumber. The two-dimensional modes are (4,0), (2,0) and (1,0), where (4,0) is the most unstable mode with wavelength equal to $L/4$. The subharmonic modes (2,0) and (1,0) initiate vortex pairings. Three-dimensionality is introduced by adding the oblique mode disturbances (4,4), $(4,-4)$, (2,2), $(2,-2)$, (1,1) and $(1,-1)$. Furthermore, random phase shifts in the oblique modes remove the symmetry in the initial conditions. Following Moser & Rogers (1993) the amplitude of the disturbances is large (0.05 for the two-dimensional and 0.15 for the three-dimensional modes).

The Reynolds number Re based on upper-stream velocity and half the initial vorticity thickness equals 50. It is sufficiently high to allow a mixing transition to small scales as observed in the incompressible simulations by Comte *et al.* (1992) and Moser & Rogers (1993). On the other hand it is sufficiently low to enable an accurate DNS that resolves all relevant turbulent scales on the computational mesh.

The DNS is conducted on a uniform grid with 192^3 cells. The accuracy of this simulation is found satisfactory. In particular the linear growth rates of the dominant instability modes are captured within 1%. Furthermore, very similar results are obtained from a simulation using a coarser grid with 128^3 cells (as shown in Vreman 1995). The time step of the explicit four-stage method equals 0.022, which is required for stability purposes. It is much smaller than needed for an accurate temporal evolution of the smallest scales.

Visualization of the DNS demonstrates the roll-up of the fundamental instability and successive pairings (figure 1). Four rollers with mainly negative spanwise vorticity are observed at $t = 20$. After the first pairing ($t = 40$) the flow has become highly three-dimensional. Another pairing ($t = 80$), yields a single roller in which the flow exhibits a complex structure, with many regions of positive spanwise vorticity. This structure is an effect of the transition to turbulence which has been triggered by the pairing process at $t = 40$ (Moser & Rogers 1993). Hence, the flow clearly contains a cascade towards small scales and all relevant scales are accurately represented on the fine grid. The simulation is stopped at $t = 100$, since the single roller at $t = 80$ cannot undergo another pairing.

In order to perform LES we solve the filtered Navier–Stokes equations closed with a subgrid model for the turbulent stress tensor. The boundary conditions for the filtered variables are the same as for their unfiltered counterparts. The initial conditions are obtained by filtering the initial conditions of the DNS described above. The simulations are performed with a filter width $\Delta = L/16$ on a uniform grid with 32^3 cells, which is considerably coarser than the DNS grid. The time step following from a stability analysis equals 0.14. The integration which appears in the definition of the filter operation is performed with the trapezoidal rule.

A consistent comparison between LES and DNS data requires filtering of the solution obtained with DNS. In order to obtain filtered DNS results, the filter operation is applied to the variables on the fine grid. Next, the filtered data are easily obtained on the coarse LES grid (being a subset of the fine DNS grid) through restriction of the filtered fine-grid data. Accurate LES results should be close to the filtered DNS results. Even if a 'perfect' LES model is adopted, exact agreement between LES and filtered DNS results cannot be expected for all types of quantities. A number of different unfiltered initial conditions defined on a fine grid can correspond to the same filtered initial condition defined on a coarse grid.

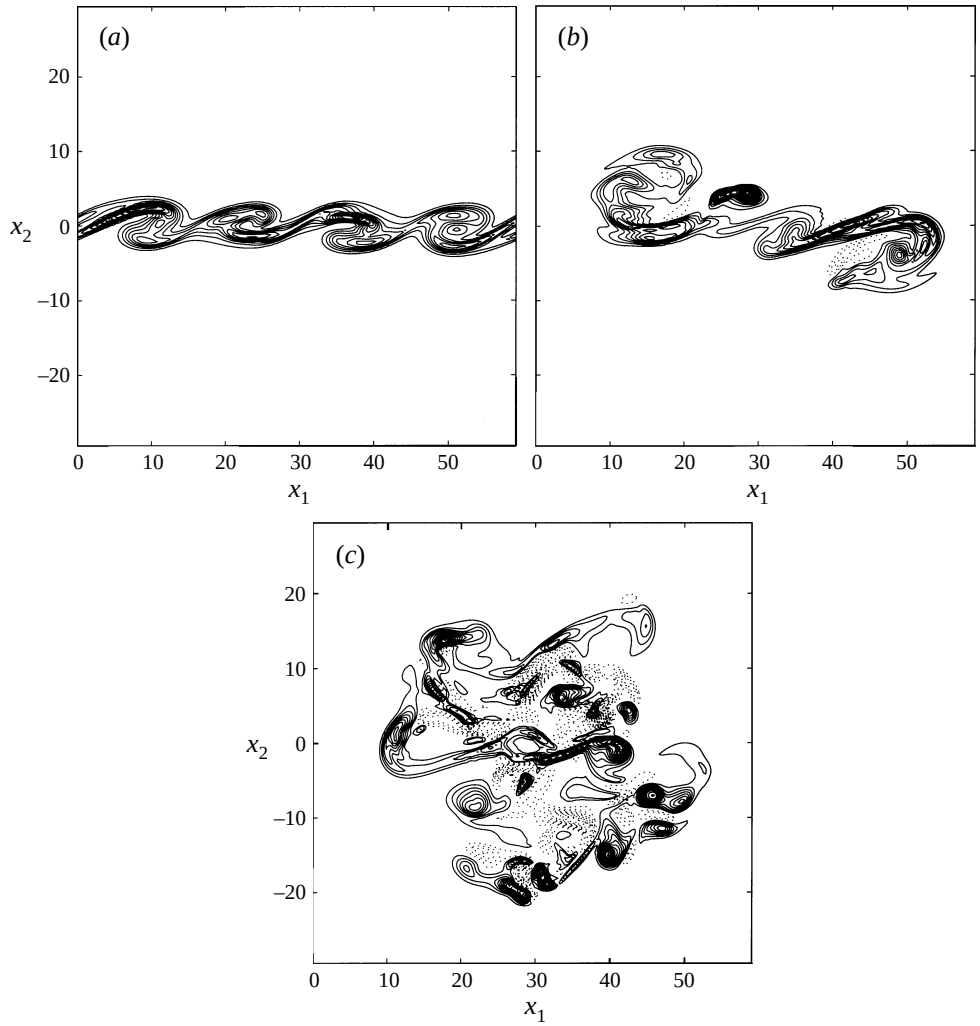

FIGURE 1. Contours of spanwise vorticity from DNS for the plane $x_3 = 0.75L$ at (*a*) $t = 20$, (*b*) $t = 40$ and (*c*) $t = 80$. Solid and dotted contours indicate negative and positive vorticity respectively. The contour increment is 0.1.

In general the DNS starting from these unfiltered initial conditions will not lead to exactly the same filtered DNS results. The agreement between LES and filtered DNS results for averaged quantities is likely to be higher than for instantaneous quantities. Hence, good quantitative agreement between accurate LES and filtered DNS results is demanded for averaged quantities and global features, rather than for instantaneous quantities, such as the evolution of the velocity at a specific location.

LES are performed using the six subgrid models for τ_{ij} formulated in § 2.2. The performance of a specific subgrid model is considered to be bad if the errors (deviations from the filtered DNS) are comparable to or larger than the errors corresponding to M0 (no subgrid model). In such a case the incorporation of the subgrid model does not make sense. For most quantities the discrepancy between the coarse-grid simulation without a subgrid model and the filtered DNS is quite large,

illustrating that there is something to improve upon; the contribution of a subgrid model should be significant.

3.2. *Comparison of results*

Various quantities obtained from LES with M0–6 are shown and compared with the filtered DNS data. We consider several aspects of the kinetic energy in detail: the evolution of total kinetic energy, turbulent and molecular dissipation, backscatter and Fourier energy spectra. The turbulent stress tensor accounts for the transfer of kinetic energy from resolved to subgrid scales. Some of the selected models adopt the eddy-viscosity hypothesis in order to approximate the energy transfer to subgrid scales. In contrast to these models, non-eddy-viscosity models (e.g. similarity) can have mechanisms to produce backscatter of energy from subgrid to resolved scales. For these models the amount of backscatter will be calculated. Furthermore, as a local quantity the spanwise vorticity in a representative plane serves to monitor the local qualitative performance of the six models. We also investigate the evolution of the momentum thickness and various averaged statistics, e.g. Reynolds-stress profiles. In this way a number of essentially different quantities (mean, local, plane averaged) are included in the *a posteriori* tests in order to assess the quality of the models.

3.2.1. *Total kinetic energy*

A comparison of the subgrid models with respect to the evolution of the total kinetic energy, based on filtered variables,

$$E = \int_{\Omega} \tfrac{1}{2}\bar{\rho}\tilde{u}_i\tilde{u}_i \mathrm{d}\boldsymbol{x}, \tag{3.1}$$

is given in figure 2. First we discuss the Smagorinsky model M1, which gives even worse predictions than M0. The total kinetic energy E for M1 is observed to exhibit a characteristic behaviour: in the transitional regime of the simulation the dissipation of energy is far too large, while it is far too low afterwards. M1 gives such an excessive dissipation in the transitional regime that the transition to turbulence is hindered. The excessive dissipation caused by this model has also been observed by Piomelli *et al.* (1990*a*) in their study of turbulent channel flow. The other models (M2–6) are not too dissipative in the transitional regime. The M3 case gives no improvement over M0, but M2 and M4–6 do improve the results. In contrast to M3, no limiter is required to stabilize M2. Comparison of the curves of M2 and M0 in figure 2 shows that the similarity model M2 dissipates approximately the correct amount of energy. As will be shown below, the simulation with M2 does not provide sufficient dissipation for small scales, although the total dissipation is reasonably well predicted. The results for M4, the dynamic eddy-viscosity model by Germano *et al.*, illustrate that the dynamic adjustment of the model coefficient meets the major shortcoming of Smagorinsky's model, namely the excessive dissipation in the transitional regime. Indeed the results are much better than those of M1. The dynamic mixed model M5 and the dynamic Clark model M6 both accurately predict the evolution of E. Within the group of models considered, M5 most closely approaches the filtered DNS results.

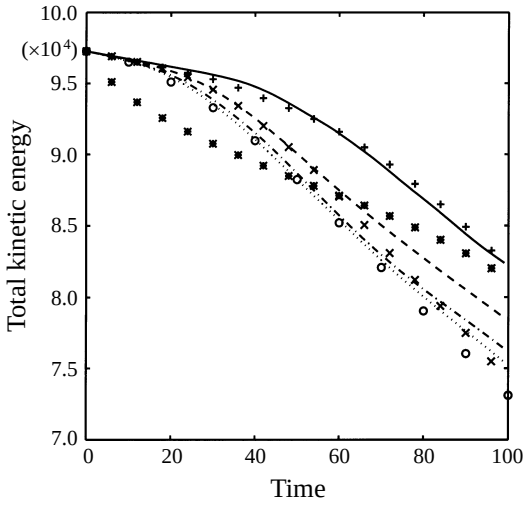

FIGURE 2. Comparison of the total kinetic energy E obtained from the filtered DNS (○) and from LES using M0–6 (see table 1 for symbols).

3.2.2. *Turbulent and molecular dissipation*

The decay of the total kinetic energy, E, is described by the following partial differential equation:

$$\partial_t E = \int_\Omega (P_d - \epsilon_\mu - \epsilon_{sgs}) \mathrm{d}\boldsymbol{x}, \tag{3.2}$$

where

$$P_d = \bar{p}\partial_k \tilde{u}_k, \tag{3.3}$$

$$\epsilon_\mu = \tilde{\mu}\tilde{S}_{ij}\partial_j \tilde{u}_i, \tag{3.4}$$

$$\epsilon_{sgs} = -\bar{\rho}\tau_{ij}\partial_j \tilde{u}_i. \tag{3.5}$$

In our case the contribution of the pressure dilatation P_d can be neglected, since the flow is almost incompressible. The molecular dissipation, ϵ_μ, is always positive due to the equality $\tilde{S}_{ij}\partial_j \tilde{u}_i = \frac{1}{2}\tilde{S}_{ij}^2$. The subgrid dissipation, ϵ_{sgs}, represents the amount of energy transferred from resolved to subgrid scales, which is positive if an eddy-viscosity model is adopted for τ_{ij}. For non-eddy-viscosity models, however, this term can be positive or negative, referring to forward or backscatter of subgrid-scale kinetic energy respectively. Backscatter produced by subgrid-models is sometimes hard to control within a simulation and can lead to numerical instability. From the models we consider, the gradient model (M3), as formulated in equation (2.11), leads to instabilities if the backscatter is not prevented with the use of a limiter (§2.2.3).

Thus, the decay of total kinetic energy is caused by both subgrid-scale and molecular dissipation. The subgrid-scale dissipation and molecular dissipation integrated over the domain are shown in figure 3. Simulation M0 is not found in figure 3(a): it has no subgrid-scale dissipation, since no subgrid-model is adopted. Figure 3(a) clearly reveals the excessive dissipation of M1 in the transitional regime. For the other models the subgrid-scale dissipation is initially small, whereas it grows when the flow undergoes the transition to turbulence. Furthermore, M2 (without limiter) and M3 (with limiter) are observed to dissipate energy, although these models do not employ

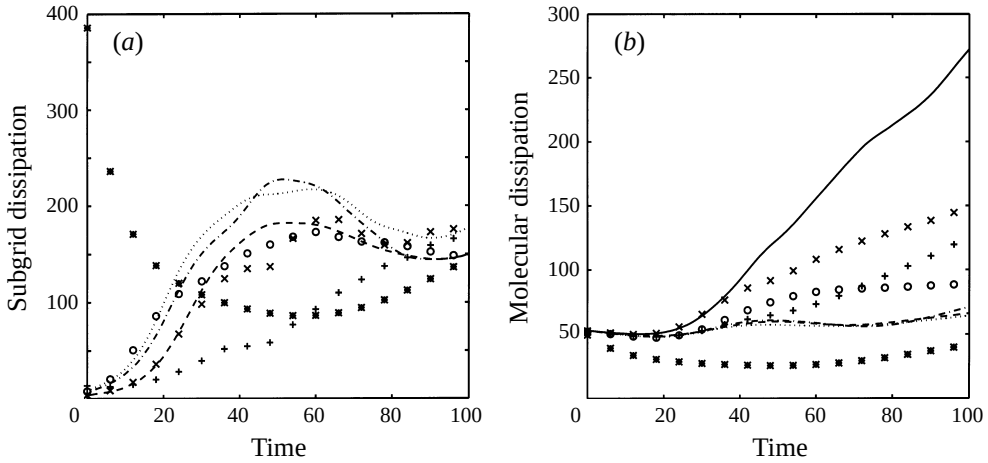

FIGURE 3. Comparison of the subgrid-scale dissipation $\int_\Omega \epsilon_{sgs} \mathrm{d}\boldsymbol{x}$ (*a*) and molecular dissipation $\int_\Omega \epsilon_\mu \mathrm{d}\boldsymbol{x}$ (*b*) obtained from the filtered DNS (marker ○) and from LES using M1–6 (see table 1 for symbols).

an eddy–viscosity. Compared to the filtered DNS results, the subgrid dissipation is reasonably well predicted by M2 and M4–6.

The simulations that employ an eddy viscosity (M1, M4–6) produce an almost constant level of molecular dissipation, whereas the molecular dissipation increases and becomes too large for M0, M2 and M3. The presence of too many small scales leads to the over-predicted molecular dissipation. In this way the molecular dissipation takes over part of the work that should be performed by the subgrid model. Obviously, the simulation with M0 is expected to contain too many small scales, since there is no subgrid model to transfer energy to subgrid scales. As will be shown in §3.2.4, the simulations with the models M2 and M3 also contain too many small scales. The amount of small-scale energy dissipated by the subgrid model is insufficient in case M2 and M3.

With respect to the dynamic models M4–6 the subgrid dissipation in the turbulent regime is best approximated by M4. The molecular dissipation is somewhat too small for all three models. The subgrid dissipation for M5–6 is somewhat too large. Consequently, the total energy decay for M5–6 is approximately correct and better than for M4. This cancellation of errors in subgrid and molecular dissipation will not occur in flows at very high Reynolds number, since in such flows the molecular dissipation is negligible compared to the subgrid dissipation. From the curves in figure 3 for the filtered DNS results and M4–6, it is inferred that in the turbulent regime of this flow the ratio between subgrid-scale dissipation and molecular dissipation is about 2 to 3, which is comparable to ratios reported in Piomelli *et al.* (1990*b*). Although this mixing layer contains a mixing transition to small-scale turbulence, the Reynolds number is relatively low. The molecular dissipation of resolved scales (ϵ_μ) will decrease if the Reynolds number is increased. A larger part of the dissipation will occur at subgrid scales since dissipation is essentially a small-scale phenomenon. Thus in high-Reynolds-number LES the somewhat over-predicted subgrid dissipation of M5–6 will not be compensated by the under-predicted molecular dissipation. Hence, in high-Reynolds-number LES the total dissipation process in the turbulent regime is possibly best predicted by M4 (see §4).

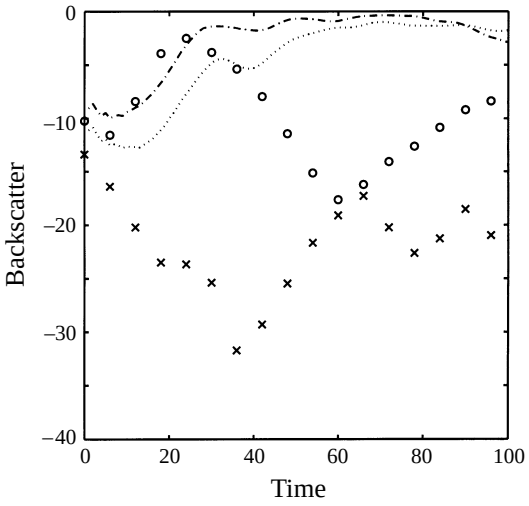

FIGURE 4. Comparison of the amount of backscatter obtained from the filtered DNS (○) and from LES using M2, M5 and M6 (see table 1 for symbols).

Figures 2, 3 and 4 can be used to verify that the dissipation caused by the numerical scheme is small. The convective terms in the continuity and the momentum equations give rise to the following term on the right-hand side of the equation for the total kinetic energy (3.2):

$$-\int_{\Omega}(\tilde{u}_i\partial_j(\overline{\rho}\tilde{u}_i\tilde{u}_j)-\tfrac{1}{2}\tilde{u}_i\tilde{u}_i\partial_j(\overline{\rho}\tilde{u}_j))\mathrm{d}\boldsymbol{x}. \tag{3.6}$$

Analytically this term can be rewritten in divergence form, $\partial_j(\frac{1}{2}\overline{\rho}\tilde{u}_i\tilde{u}_i\tilde{u}_j)$, which yields zero after integration over the flow domain. Numerically, however, this term is not zero and measures the amount of numerical dissipation (it would be zero for a so-called 'kinetic energy conserving' scheme). We illustrate this for the simulation with M5 and integrate equation (3.2) over time. The total decay of kinetic energy ($E(t=0)-E(t=100)$) equals 22 068 (figure 2). Integration of the right-hand side of (3.2) yields 21 170 for subgrid and molecular dissipation (figure 3) and 128 for the dissipation caused by the pressure dilatation term. Hence the numerical dissipation is 770, which is only 3.5% of the total dissipation. (We have checked that the effects due to the discretization in time and rewriting P_d, ϵ_{sgs} and ϵ_μ are negligible.) For the other dynamic models the numerical dissipation has almost the same value. The numerical dissipation is largest in the no-model case (1564), due to the large amount of under-resolved small scales, but it is still small compared to the molecular dissipation (13 360). It appears that if the subgrid dissipation is adequately handled by the subgrid model, the numerical dissipation with the present numerical scheme is sufficiently small.

3.2.3. *Backscatter*

The amount of backscatter produced by several subgrid models is addressed next. The eddy-viscosity models M1 and M4 do not produce backscatter since the model coefficient in M1 is a positive constant by definition and the dynamic model coefficient in M4 is restricted to positive values in order to ensure numerical stability. Moreover, the limiter concept in M3 artificially removes the backscatter from this model. Therefore, the only models which produce backscatter are M2, M5 and M6.

For these models the total amount of backscatter, defined as

$$\int_{\Omega} \min(\epsilon_{sgs}, 0) \mathrm{d}\boldsymbol{x}, \tag{3.7}$$

is plotted in figure 4. Since M5–6 incorporate an eddy-viscosity, these models produce less backscatter than M2. The amount of backscatter for M5–6 is relatively low in the turbulent regime, where the eddy-viscosity part of the model is more important than in the transitional regime. A comparison with the filtered DNS results shows that M2 produces too much backscatter, whereas M5–6 do not produce enough backscatter. Except in the early stages of the simulation, the amount of backscatter is only a small fraction of the forward scatter (about 10% for the filtered DNS results). *A priori* tests of transitional and turbulent channel flow show comparable back- and forward scatter for the spectral cut-off filter, but smaller back- than forward scatter for the top-hat and Gaussian filters (Piomelli *et al.* 1990*b*). Here *a posteriori* tests of the mixing layer demonstrate that in the filtered DNS on a coarse grid and in actual LES with the top-hat filter the structure of the turbulent flow is such that the amount of backscatter is relatively small. In a recent study on dynamic LES of isotropic turbulence, taking backscatter into account did not significantly influence the results either (Carati, Ghosal & Moin 1995).

Others decompose the subgrid dissipation ϵ_{sgs} into a mean and a fluctuating part (Jiménez-Härtel 1994; Horiuti 1995) and find that the amount of backscatter in the fluctuating part is relatively large. In this subsection we focused on the importance of backscatter relative to the full dissipation of energy to subgrid scales.

3.2.4. *Magnitude of turbulent stress*

In this subsection we turn to the prediction of the separate components of the turbulent stress. We restrict the presentation to the τ_{12} component, but similar conclusions hold for the other components as well.

The L_2-norm of the τ_{12} component of the turbulent stress tensor is plotted in figure 5. Model M1 strongly over-predicts the magnitude in the transitional regime. The prediction of the similarity model M2 is better than of the gradient model M3 and is of all models closest to the filtered DNS results. The turbulent stress in the dynamic eddy-viscosity model is much too small: it is less than half the filtered DNS value. The dynamic mixed models M5 and M6 also under-predict the real magnitude of τ_{12}, but compared to M4 the curves are much closer to the filtered DNS result.

To further analyse the behaviour of the dynamic mixed and Clark models the L_2-norms of the separate components of M5 and M6 as models for τ_{12} are plotted in figure 6(*a*). The similarity and gradient components clearly dominate in the L_2-norm of τ_{12}; the L_2-norms of these parts are only slightly smaller than the norms of the sums (with the eddy-viscosity parts added). With respect to the contribution to the subgrid dissipation (figure 6*b*) the picture is completely different: the eddy-viscosity parts contribute more to the dissipation than the similarity and gradient parts. These *a posteriori* findings are in agreement with the *a priori* findings reported by Liu *et al.* (1994*a*). The explanation of this behaviour is obvious: the eddy-viscosity parts is aligned with the strain rate (by definition), the similarity and gradient parts are not and neither is the real turbulent stress tensor. A more remarkable observation is that the dynamic eddy-viscosity model gives the proper subgrid dissipation, but under-predicts the turbulent stresses. This situation is more desirable than a situation in which the magnitude of the turbulent stresses is correctly modelled, but the subgrid dissipation is much too large. This case would occur if the dynamic formulation forced a correct

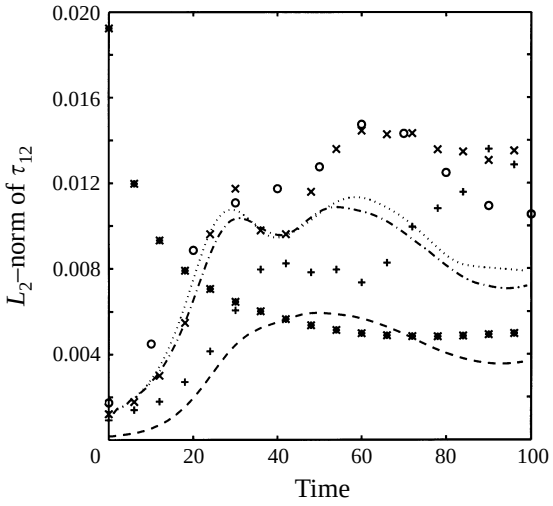

FIGURE 5. Comparison of the L_2-norm of τ_{12} obtained from the filtered DNS (○) and from LES using M1–6 (see table 1 for symbols).

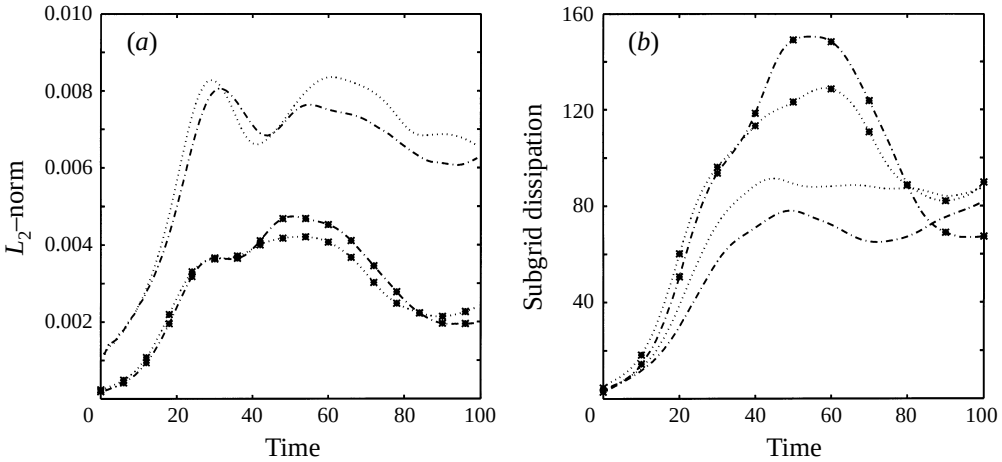

FIGURE 6. L_2-norms of contributions to τ_{12} (*a*) and integrated contributions to ϵ_{sgs} (*b*): the similarity part of M5 (dotted), the eddy-viscosity part of M5 (dotted, marker ∗), the gradient part of M6 (dashed-dotted) and the eddy-viscosity part of M6 (dashed-dotted, ∗).

prediction of the magnitude of the individual components of the turbulent stress tensor. If good estimates of the individual components are required, the dynamic mixed and Clark models are preferred over the dynamic eddy-viscosity model, because they give reasonable magnitudes of the turbulent stresses in combination with a proper dissipative behaviour.

3.2.5. *Energy spectrum*

We mentioned that the increase in molecular dissipation observed for M0, M2 and M3 was due to the presence of small scales. This is further clarified by examination of the energy spectrum at a certain time and the time evolution of specific small- and large-scale components of the spectrum. Figure 7 contains the streamwise kinetic energy spectrum in the turbulent regime at $t = 80$, denoted by $A(k)$, where k is the

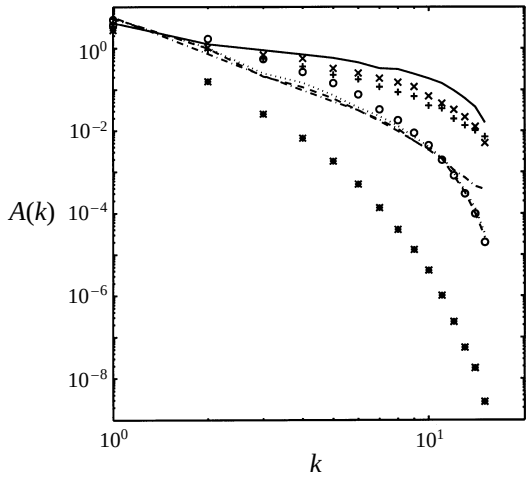

FIGURE 7. Comparison of the streamwise energy spectrum $A(k)$ at $t = 80$ obtained from the filtered DNS (○) and from LES using M0–6 (see table 1 for symbols).

streamwise wavenumber. The spanwise energy spectrum exhibits similar features. The filtered DNS result does not contain an inertial range displaying the $-5/3$-law, because the spectrum is based on the filtered velocity and the Reynolds number is relatively low in order to enable DNS. The spectrum of the filtered DNS is in good agreement with those of the dynamic models M4 and M5, with a slight preference for M5. The spectrum for the third dynamic model (M6) is too large for the highest wavenumbers. Furthermore, we observe that the simulation with M1 is not able to generate the desired amount of small scales. On the other hand, the contributions of high wavenumbers are too high for M0, M2 and M3 and, consequently, these simulations contain too many small-scale contributions. This was to be expected for M0, having no subgrid was model, whereas this result indicates insufficient energy dissipation of small scales for M2 and M3.

3.2.6. *Spanwise vorticity in a plane*

The spanwise vorticity component is often used to visualize the large-scale roller structure in mixing layers at low Mach number. In figure 1 we have visualized the scenario for the DNS: four rollers of spanwise vorticity at $t = 20$, two at $t = 40$ and one at $t = 80$. During these pairing processes the mixing layer undergoes a transition to turbulence and many small regions of spanwise vorticity of both signs occur. In the LES this scenario is reproduced in nearly all cases (M0, M2–6). Only the simulation with the Smagorinsky model M1 is an exception: instead of four rollers at $t = 20$ only two rollers form, indicating that the linear instability process is highly affected by the excessive dissipation caused by M1. Figure 8 displays the spanwise vorticity at $t = 80$ in the plane $x_3 = 0.75L_3$ for the filtered DNS restricted to the coarse grid and for M0–6. First, we compare the filtered DNS result in figure 8(a) with the unfiltered DNS result in figure 1(c), which corresponds to the same time and plane. Obviously, the smallest structures are removed by the filtering and the peak values of the vorticity are considerably reduced. The vorticity field of the filtered variables can successfully be represented on the coarse grid. Furthermore, the amount of positive spanwise vorticity in the filtered case is smaller than in the unfiltered result. We

conclude that most structures of positive spanwise vorticity in the DNS are smaller than the filter width Δ, thus being subgrid scales on the LES grid.

In the following, we turn to the LES predictions of M0–6 in figure 8(*b–h*), which ideally should resemble the filtered DNS result in figure 8(*a*). The simulation with no subgrid model (figure 8*b*), contains too many small-scale structures and the peak intensities are too large. The physical dynamics of such small-scale structures clearly cannot be correctly captured on the coarse 32^3-grid. On the other hand the result in figure 8(*c*), corresponding to the Smagorinsky model M1, is too smooth; it contains mainly large-scale structures. The two rollers produced at $t = 20$ (instead of four) have slowly started to pair at $t = 80$, but no transition to smaller scales occurs and the mixing layer is much too thin. Like M0, the similarity model (M2, figure 8*d*) and gradient model (M3, figure 8*e*) give rise to an excessive number of small structures and regions of positive spanwise vorticity. This is in agreement with the energy spectra in figure 7, in which the contributions at high wavenumbers are too large. Furthermore, the vorticity distribution of M2 is quite similar to M0, only the peak intensities for M2 are weaker. Figure 8(*e*) clearly shows that M3 under-predicts the thickness of the layer.

The vorticity obtained with the dynamic models (M4–6 in figure 8*f–h*) is qualitatively in better agreement with the filtered DNS results than the previous plots. The peak values of the vorticity are quite well predicted and almost the correct amount of small structure is present. With respect to the dynamic models, M5 is preferred over M4 and M6. The thickness of the mixing layer is better predicted by M5 than by M4. Furthermore, compared to M4 and M6, more regions of positive spanwise vorticity are present and the negative regions are less connected, which is in agreement with figure 8(*a*). Hence, M5 yields the best qualitative agreement with the filtered DNS. As explained in §3.1 detailed agreement between LES and filtered DNS on a local instantaneous level is not required.

The structure obtained with M5 (figure 8*g*) is more elongated in the x_1-direction than the filtered DNS structure in figure 8a. The spanwise vorticity of the M5 LES in other planes at $t = 80$ (e.g. $x_3 = L$), however, shows much rounder structures. Furthermore, a more 'rolled-up' structure in the same plane ($x_3 = 0.75L$) is found at a later time ($t = 85$). Compared to the filtered DNS, the pairing process and the growth of the shear layer are somewhat delayed in LES with M5 (see also figure 10).

3.2.7. *Positive spanwise vorticity*

The occurrence of positive spanwise vorticity in the mixing layer is related to the transition to turbulence. Due to the mean profile, the spanwise vorticity is initially negative in the whole domain. In the two-dimensional case such an initial condition implies that the (spanwise) vorticity remains negative throughout the simulation. Apart from compressibility effects, only the 'vortex-stretching' term in the vorticity equation can increase the global maximum of a vorticity component. Vortex stretching is essential in the generation of turbulence. From examining the evolution of the maxima (or minima) of vorticity components it can be inferred whether this mechanism is present in the flow.

In figure 9 the evolution of the maximum of the spanwise vorticity is shown for the various simulations considered. The filtering strongly reduces the DNS values for this quantity, as is observed from a comparison of figures 1(*c*) and 8(*a*), but figure 9 shows that the sudden increase of positive spanwise vorticity is also present in the filtered DNS. The models M0, M2 and M3 over-predict this quantity, since in these simulations there are too many small-scale contributions. On the other hand,

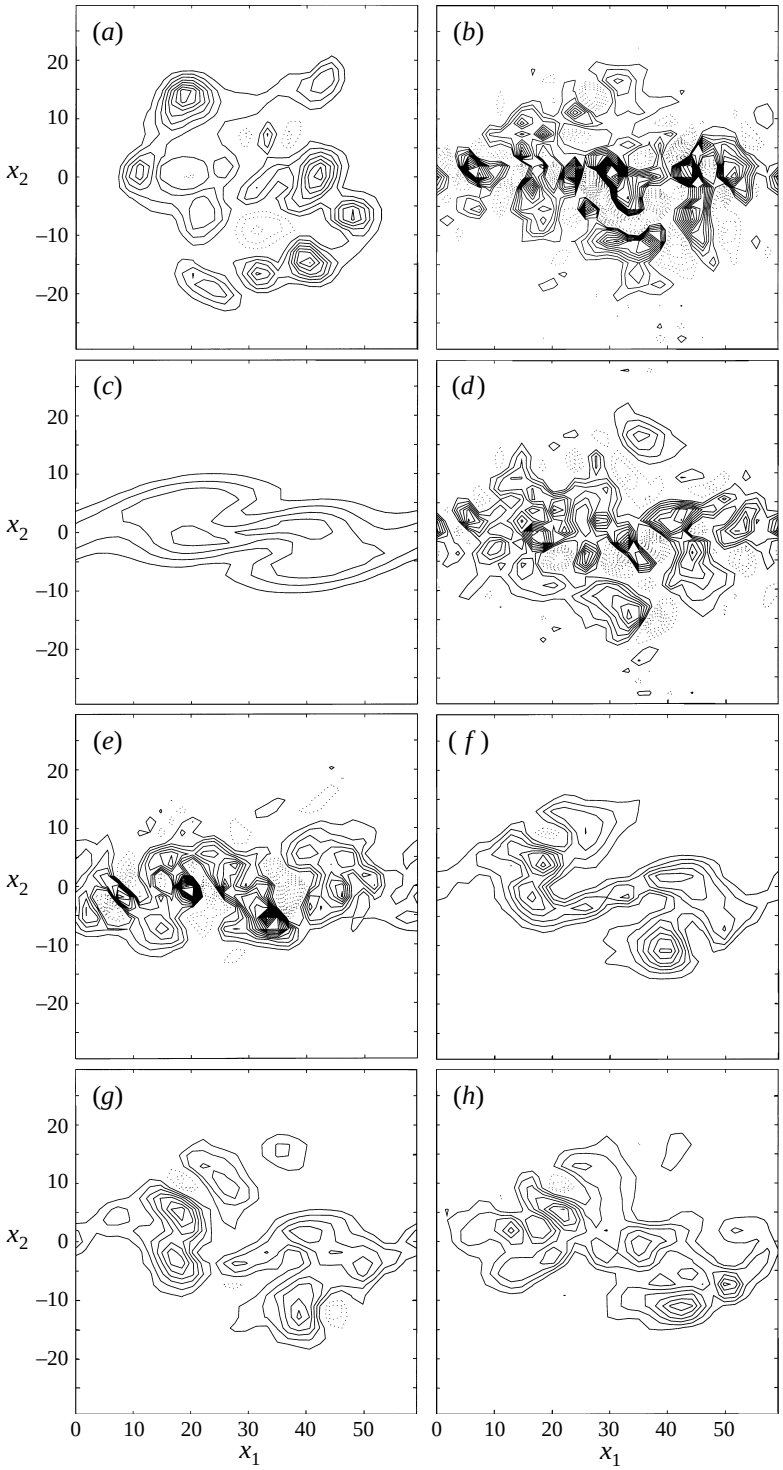

FIGURE 8. Contours of spanwise vorticity for the plane $x_3 = 0.75L$ at $t = 80$ obtained from (*a*) the filtered DNS, restricted to the 32^3-grid, and from LES using (*b*) M0, (*c*) M1, (*d*) M2, (*e*) M3, (*f*) M4, (*g*) M5 and (*h*) M6. Solid and dotted contours indicate negative and positive vorticity respectively. The contour increment is 0.05.

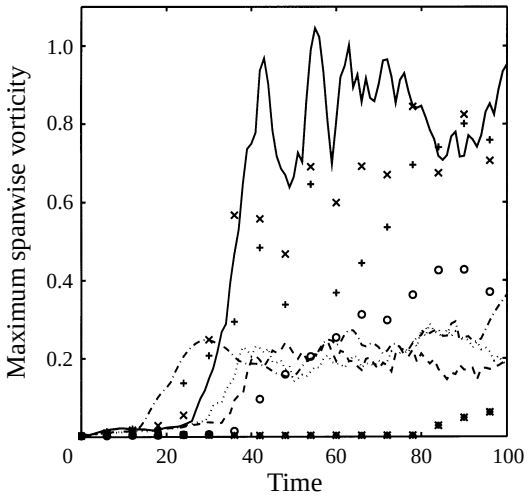

FIGURE 9. Comparison of the spatial maximum of positive spanwise vorticity as a function of time obtained from the filtered DNS (○) and from LES using M0–6 (see table 1 for symbols).

in the simulation with M1 no positive spanwise vorticity is generated for a long time, corresponding to the absence of strong vortex stretching. This result again illustrates that the Smagorinsky model hinders the transition to turbulence. The dynamic models M4 and M5 both give predictions which are relatively close to the filtered DNS results, whereas the increase of positive spanwise vorticity starts too early for M6.

3.2.8. *Momentum thickness*

From figure 8 we have already observed that the thickness of the mixing layer depends on the subgrid model. This dependence is further clarified in figure 10, in which the evolution of the momentum thickness, based on filtered variables,

$$\delta = \tfrac{1}{4}\int_{-L/2}^{L/2} \langle\bar{\rho}\rangle \left(1 - \frac{\langle\bar{\rho}\tilde{u}_1\rangle}{\langle\bar{\rho}\rangle}\right)\left(\frac{\langle\bar{\rho}\tilde{u}_1\rangle}{\langle\bar{\rho}\rangle} + 1\right) \mathrm{d}x_2, \tag{3.8}$$

is shown. The operator $\langle . \rangle$ represents an averaging over the homogeneous directions x_1 and x_3. Since the definition of the momentum thickness employs the mean velocity profile, tests for the momentum thickness quantify the spreading of the mean velocity profile. Figure 9 displays a short period of laminar growth (until $t = 20$), followed by a period in which the mixing layer grows considerably faster, visualizing the increased mixing caused by turbulence.

The models M1 and M3 lead to worse predictions for the momentum thickness than M0, indicating that with respect to this quantity LES without a subgrid model is preferred over adopting M1 or M3. The slow growth of the momentum thickness for M1 further establishes the observation that this model hinders the transition to turbulence. The results for M4 are quite similar to M0, whereas the models M2, M5 and M6 clearly yield improvement over M0 and are relatively close to the filtered DNS result. It is remarkable that the evolution of the momentum thickness is almost identical for M2 and M5. This indicates that for the momentum thickness the improvement over M0 is mainly due to the similarity model, since the eddy viscosity part of M5 does not seem to affect this quantity. Other evidence for the small effect

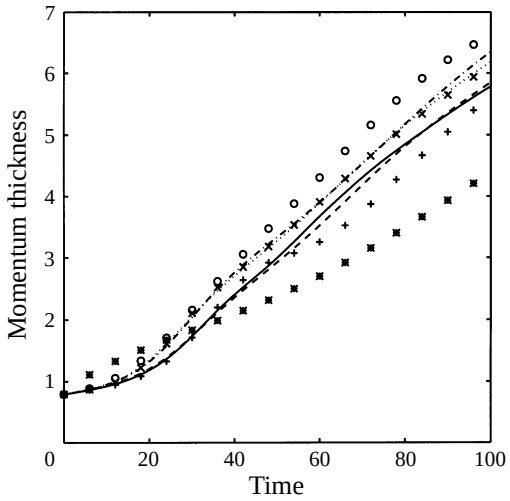

FIGURE 10. Comparison of the momentum thickness obtained from the filtered DNS (○) and from LES using M0–6 (see table 1 for symbols).

of the dynamic eddy viscosity on the momentum thickness is that the curves for M0 and M4 almost coincide. The similarity model, however, already plays a role in the early stages of transition. The time at which the increased mixing starts is relatively early compared to M0. This behaviour is confirmed by the finding that growth rates of linear instability waves are increased by the similarity model and are also closer to the correct values.

3.2.9. *Profiles of averaged statistics*

Finally, we will compare x_2-profiles of various statistics averaged in the homogeneous directions. These profiles will be calculated at $t = 70$, which is well beyond the starting point of the mixing transition process, but just before the final pairing has been accomplished. In the definition of these profiles, $v_i = \tilde{u}_i - \langle\bar{\rho}\tilde{u}_i\rangle/\langle\bar{\rho}\rangle$ denotes a fluctuating velocity field. In figure 11(*a–c*) the turbulent intensities $\langle\bar{\rho}v_i^2\rangle^{1/2}$ are shown for $i = 1, 2, 3$. The filtered DNS results demonstrate that the streamwise intensity is somewhat larger than the normal and spanwise intensities. The turbulent intensities are too large for M0, while they are under-predicted by M1; M3 gives reasonable predictions for $i = 2$, but the peak for $i = 1$ is much too high, whereas the spreading for $i = 3$ is too low. The remaining three models (M2, M4–6) are equally accurate; the global discrepancies with the filtered DNS results are approximately the same, although M6 is slightly better than the other models for $i = 1$. With respect to the Reynolds stress profile $-\langle\bar{\rho}v_1v_2\rangle$, shown in figure 11(*d*), the dynamic mixed model M5 has to be preferred, since it provides the most accurate approximation of the filtered DNS profile.

3.2.10. *Summary and discussion*

Table 2 summarizes the results for the subgrid models M1–6. The discrepancy with the filtered DNS determines the quality of the result. In general, a result for a given subgrid model is considered to be bad if its discrepancy with the filtered DNS is larger than that between the filtered DNS and M0. If within a group of models that provide good results denoted by '+', one model performs even better than the others, it is labelled with '++'. Simulations with M2 and M4–6 do give considerable

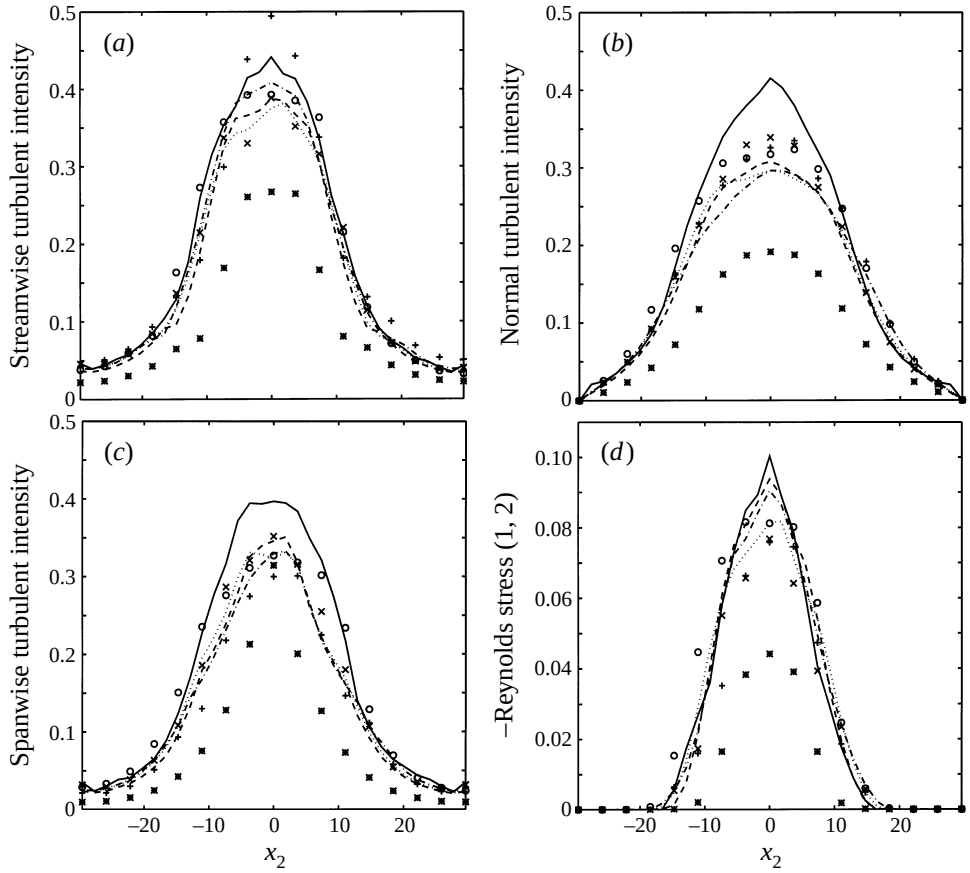

FIGURE 11. Comparison of the profiles of the turbulent intensities $\langle \bar{\rho} v_i^2 \rangle^{1/2}$ for $i = 1, 2, 3$ (a, b, c) and the Reynolds stress $-\langle \bar{\rho} v_1 v_2 \rangle$ (d) at $t = 70$ obtained from the filtered DNS (o) and from LES using M0–6 (see table 1 for symbols).

improvements over M0; the incorporation of these models is useful in LES of the mixing layer. Within the group of these four models, the dynamic mixed model (M5) provides the most accurate results, compared to the filtered DNS results. Table 2 further shows that with respect to overall accuracy M6 is next to M5, then M4 and then M2.

The subgrid models studied in this paper are based on the notion of similarity and the need to represent the energy transfer to the subgrid scales through the introduction of dissipation. The latter is required since the filtering operation removes the dissipative scales. Models which do not explicitly contain dissipation (M2, M3) indeed do not capture the correct energy transfer and consequently display too much molecular dissipation. Conversely, the Smagorinsky model has no mechanism to determine the proper amount of subgrid-scale dissipation. However, such a mechanism can be provided by the similarity hypothesis.

The assumption of similarity implies that the turbulent stresses display a univeral behaviour in the inertial subrange. This assumption is not only used explicitly in the similarity and gradient models, but also implicitly in the dynamic approach. In particular, similarity justifies the use of *one* model at the different length scales appearing in the Germano identity (15) (Carati & Vanden Eijnden 1996). This

	Figure	M1	M2	M3	M4	M5	M6
Total kinetic energy	2	−	+	−	0	++	+
Subgrid dissipation	3(*a*)	−	+	−	++	+	+
Molecular dissipation	3(*b*)	−	+	+	+	+	+
Backscatter	4	−	0	−	−	0	0
Component τ_{12}	5	−	+	0	−	+	+
Energy spectrum $A(k)$	5	−	−	−	+	++	0
Vorticity in a plane	6, 7	−	−	−	+	++	+
Maximum vorticity	8	−	−	−	+	+	0
Mmomentum thickness	9	−	+	−	−	+	++
$\langle v_1 v_1 \rangle^{1/2}$	10(*a*)	−	+	−	+	+	++
$\langle v_2 v_2 \rangle^{1/2}$	10(*b*)	−	+	+	+	+	+
$\langle v_3 v_3 \rangle^{1/2}$	10(*c*)	−	+	0	+	+	+
$-\langle v_1 v_2 \rangle$	10(*d*)	−	−	−	0	++	+

TABLE 2. Summary of the results for M1–6. The symbols −,0 and + refer to bad, reasonable and good results, respectively. Furthermore, ++ is better than +.

approach has been shown to provide an accurate prediction of the subgrid dissipation (cf. M4 in figure 3*a*). In combination with an explicit similarity model (M5, M6) the dynamic approach results in a too large subgrid dissipation. This could be explained as follows. For the calculation of the tensor H_{ij} in (23) two consecutive applications of the test filter are needed. Thus the similarity assumption is required to hold over a much larger range of scales. For the larger scales this is generally less valid, leading to a too small correlation between H_{ij} and M_{ij} appearing in (24). This is consistent with the findings of Liu *et al.* (1994*b*) and leads to an over-prediction of C_d. For the Reynolds number considered in this section this over-prediction is to a large extent balanced by the under-prediction of the molecular dissipation when using a dynamic model. This suggests that model M4 performs relatively better at higher Reynolds numbers, where the molecular dissipation is even smaller. This is the subject of the next section.

We did not include results for the non-dynamic mixed model (M2 plus M1, Bardina *et al.* 1984), nor for the non-dynamic Clark model (M3 plus M1, Clark *et al.* 1979). However, we did run simulations with these models. The results were similar to those obtained with M1, in particular with respect to the excessive dissipation in the transitional period.

Each subgrid model was used in combination with the top-hat filter. The filter is explicitly used in filtering the DNS data and in LES with M2, M4, M5 and M6, but is only formally used in M1 and M3. Piomelli, Moin & Ferziger (1988) compared the spectral cut-off and the Gaussian filter in combination with several models and they advise using M1 with the spectral cut-off and the mixed model (non-dynamic version of M5) with the Gaussian filter. The Gaussian and top-hat filter are very similar (see the Appendix and Vreman *et al.* 1994*a*) and we verified that results of the M4 and M5 simulations do not change much if we use the Gaussian filter instead of top-hat. In M1 the filter is not explicitly used; hence the conclusion that this model is excessively dissipative during transition would not change for a spectral filter, even if the results were compared with spectrally filtered DNS data.

The 32^3-grid is not too coarse for proper *a posteriori* tests. The results in this paper show that LES on this grid is in satisfactory agreement with the filtered DNS, provided an appropriate subgrid model is used. The results would of course be better if we

increased the resolution to 64^3, but then even the coarse-grid DNS (M0) would give reasonable results and the subgrid dissipation would not be larger than the molecular dissipation. Using the 32^3-grid, however, the subgrid dissipation is about three times higher than the molecular dissipation (figure 3), indicating that a subgrid model is needed, since the largest part of the dissipation is caused by the small subgrid eddies. On the other hand the 32^3 grid is sufficiently fine to discern the largest eddies, namely the four spanwise rollers, subsequently pairing to two, and finally to one roller. The resolution of 32 uniformly spaced points in the normal direction on a uniform grid is not too small for the representation of the mean profile, which can be concluded from the following arguments. Firstly, we have repeated the full comparison on a LES grid of $32 \times 64 \times 32$ points and this set of simulations confirmed the findings in this section. Secondly, it has to be noticed that according to the definition of the initial conditions in LES, *filtered* mean profiles are used, which are smoother than the original mean profiles. The instability resulting from this profile is essentially the same as in the filtered DNS, since for all models considered (except for M1) LES on the 32^3-grid was observed to reproduce the four-roller structure that results from the primary instability. Furthermore, the flow structure in the turbulent regime (e.g. figures 1*c*, 8) suggests the choice of equal grid sizes in all three directions.

4. Self-similarity

In this section we perform LES of the temporal mixing layer at a higher Reynolds number and in a larger domain using the subgrid models M0–6. Although the simulation described in §3 contained a transition to small scales, the size of the domain allowed two successive pairings only and the Reynolds number was relatively low (50) in order to enable DNS. Compared to DNS, LES should be able to simulate flows in a larger domain and at higher Reynolds number at the same computational cost.

The temporal mixing layer in this section is simulated at $Re = 500$, based on the reference values defined in §2.1. The calculation is performed on a grid with 120^3 cells and the computational domain is large, $L = 120$. This size is equal to eight times the wavelength of the fundamental linear instability. Hence, the flow allows three successive pairings before it saturates. Uniform noise is used to perturb the initial mean flow (amplitude 0.05 and multiplied with $\mathrm{e}^{-x_2^2/4}$), in contrast to §3.1 where an eigenfunction perturbation was used. The LES employ the top-hat filter with the basic filter width equal to twice the grid spacing.

At this Reynolds number there are no DNS results to compare with, but we can verify whether the flow is self-similar. A temporal mixing layer is self-similar if the development of the shear layer thickness is linear in time and profiles of normalized statistical quantities at different times coincide. The common opinion is that turbulent mixing layers display self-similar behaviour, provided the Reynolds number is high and the computational domain is large and the simulation is performed sufficiently far in time (Rogers & Moser 1994; Vreman *et al.* 1996*c*). Experimental work supports the notion of similarity (Brown & Roshko 1974; Campagne, Pao & Wynanski 1976; Bell & Mehta 1990). The specific self-similar state, however, is not unique but depends on the initial forcing (Dimotakis & Brown 1976).

The evolution of the momentum thickness is shown in figure 12 for the subgrid-models M1 and M4–6. None of the simulations is fully self-similar, since in each case the momentum thickness curve is not perfectly straight in the turbulent regime. The most self-similar case is obtained with the dynamic eddy-viscosity model M4,

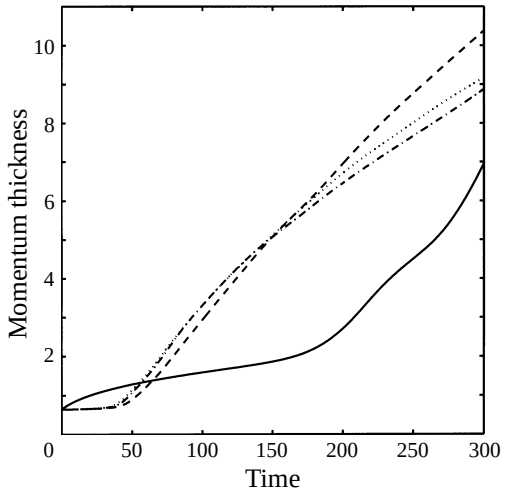

FIGURE 12. Evolution of the momentum thickness $\delta(t)$ obtained using M1 (solid), M4 (dashed), M5 (dotted) and M6 (dashed-dotted).

where $\delta(t)$ is approximately linear between $t = 100$ and 250. The other two dynamic models, M5 and M6, lead to a faster growth than M4 between $t = 40$ and 130, but to a slower growth afterwards.

Like the results in §3, the present results show that M1 is too dissipative in the laminar regime, where the laminar increase of momentum thickness is too large. Although the model does not prevent the transition to turbulent flow, the transition is delayed and the sudden growth of the momentum thickness starts relatively late (at $t = 175$). Furthermore, the momentum thickness does not increase linearly in the turbulent regime, showing that the mixing layer is not self-similar. The M1 results shown were obtained using a Smagorinsky constant of 0.17 (Lilly 1967; Schumann 1991). In order to study the sensitivity to the Smagorinsky constant we repeated the M1 simulation in this section with a lower coefficient, $C_S = 0.10$. This value was proposed by Deardorff (1970) in LES of turbulent channel flow, whereas Moin & Kim (1982) used an even lower value. Compared to the dynamic models, M1 with $C_S = 0.10$ was still much too dissipative in the first part of the simulation and the transition to turbulence was still relatively late ($t = 100$). After transition had occurred, the momentum thickness did not increase linearly, like in the simulation with $C_S = 0.17$.

Results for M0, M2 and M3 are not shown, because the simulations with these models become unstable before $t = 100$ and, therefore, cannot be completed. The reason is the insufficient dissipation from resolved to subgrid scales. We have noticed too much energy in the small scales in the simulations at lower Reynolds number (§3.2.4) and this leads to unstable simulations at high Reynolds number. We found that these simulations were also unstable with a 'kinetic energy-conserving' scheme. Even when the total kinetic energy cannot increase, there can be too much energy in the small scales, leading to instability through the thermodynamic variables (as indicated in §2.1).

The evolution of the dynamic model coefficients at $x_2 = 0$ is shown in figure 13 together with the value of C_S^2 in M1. Indeed, $C_S = 0.17$ is initially much too large and is even too large in the turbulent regime. The alternative value tested, $C_S = 0.1$ is also too large initially, but too low in the turbulent regime. The Smagorinsky coefficient

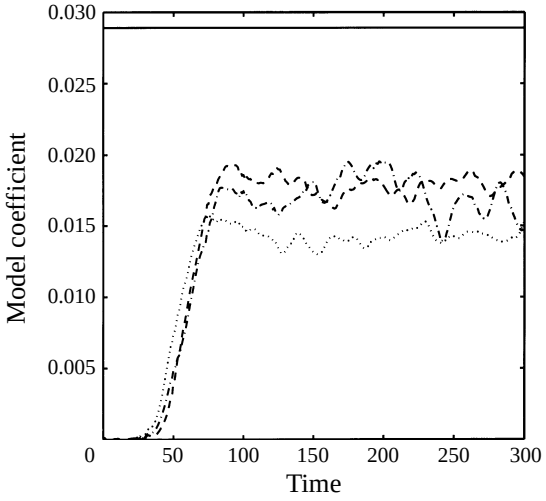

FIGURE 13. The dynamic model coefficient C_d at $x_2 = 0$ in LES with M4 (dashed), M5 (dotted) and M6 (dashed-dotted), and the value of C_S^2 in M1 (solid).

corresponding to the average value of the dynamic coefficient of M4 in the turbulent regime would be $C_S = 0.13$. The eddy viscosities in M5-6 model a part of the turbulent stress tensor only and therefore the dynamic coefficients in M5–6 are lower than in M4. However, in this case the differences between the model coefficients of M4–6 are smaller than at low Reynolds number (Vreman *et al.* 1994*b*), which implies that incorporation of a similarity or gradient part is less effective in the prediction of the subgrid dissipation if the Reynolds number is high.

Statistical quantities are self-similar if profiles at different times coincide after the appropriate normalization. In the following we consider the Reynolds stress profiles, $R_{ij} = \langle \bar{\rho} v_i v_j \rangle$, with v_i defined as in §3.2.8, and the dissipation profile $\langle \epsilon \rangle = \langle \epsilon_{sgs} + \epsilon_\mu \rangle$, with ϵ_{sgs} and ϵ_μ defined as in §3.2.2. These profiles are functions of time and the normal direction x_2, which scales with $\delta(t)$. The Reynolds stress tensor and the dissipation can be scaled by $\rho_1(\Delta U)^2$ and $\rho_1(\Delta U)^3/\delta(t)$ respectively, where ρ_1 is the upper free-stream density and ΔU is the velocity difference between the free streams.

The resolved turbulent kinetic energy $\frac{1}{2}R_{qq}$ at $x_2 = 0$ and the integrated dissipation $\int \langle \epsilon \rangle \mathrm{d}x_2$ are shown in figure 14. In self-similar flow these quantities should not depend on time. From this figure it appears that an approximate self-similar state is best reached by M4. Due to the finite size of the computational domain the statistics are expected to decay after some time, but compared to M4 the decay starts relatively early for M5–6. The somewhat over-predicted subgrid dissipation by M5–6 noticed in §3.2.2 is a possible reason for the relatively early decay. In these LES at high Reynolds number, the fraction of the dissipation due to molecular viscosity is low (less than 10% in the turbulent regime). Compared to ϵ_{sgs} the amount of backscatter generated by M5–6 at high Reynolds number is less than 0.3%, which is even smaller than at low Reynolds number (§3.2.3).

In principle self-similarity should be verified not for the resolved but for the *unfiltered* flow field. The momentum thickness is based on the mean velocity field, which is smooth and therefore hardly influenced by the use of filtered instead of unfiltered variables. With respect to the dissipation the subgrid part (ϵ_{sgs}) is dominant and was included in figure 14(*b*). In the following we also address the subgrid

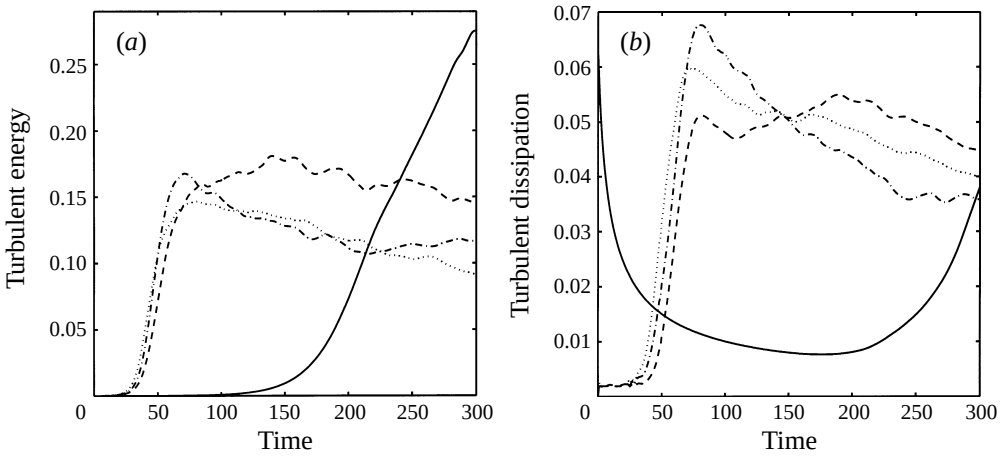

FIGURE 14. Evolution of the resolved turbulent energy $\frac{1}{2}R_{qq}$ at $x_2 = 0$ (*a*) and dissipation $\int\langle\epsilon\rangle \mathrm{d}x_2$ (*b*) obtained from LES with M1 (solid), M4 (dashed), M5 (dotted) and M6 (dashed-dotted).

contribution to the Reynolds stresses. The Reynolds stress tensor defined for unfiltered variables, $r_{ij} = \langle\rho w_i w_j\rangle$ with $w_i = u_i - \langle\rho u_i\rangle/\langle\rho\rangle$, can be related to the resolved Reynolds stress R_{ij} as follows:

$$r_{ij} \approx R_{ij} + \langle\tau_{ij}\rangle. \tag{4.1}$$

This approximation used by e.g. Deardorff (1970) is exact in incompressible flow if the LES filter is a 'generic' filter, which implies $\langle\bar{f}\rangle = \langle f\rangle$ (Germano 1996). (Using the DNS data from §3, we found that $\langle\tau_{ij}\rangle$ estimates $r_{ij} - R_{ij}$ with an error of about 10%.)

Figure 15(*a*) displays the profile of the resolved Reynolds stress R_{11} obtained with M4 at three distinct times, where $y = x_2/\delta(t)$. The curves approximately coincide, confirming that the simulation is reasonably self-similar during this period of time, even for the resolved Reynolds stress. The subgrid contribution $\langle\tau_{11}\rangle$ cannot be directly obtained from M4, because the trace τ_{qq} in M4 is not modelled and implicitly added to the pressure. Estimates for the trace in terms of the eddy viscosity exist (e.g. Deardorff 1970), but then it is still unclear which part of the trace corresponds to τ_{11}. We therefore estimate $\langle\tau_{11}\rangle$ using the similarity model for τ_{11}. The results in figure 15(*b*) show that the profiles of the subgrid contribution are not self-similar, but that at later times a relatively smaller part of the Reynolds stress is in the subgrid scales. Furthermore, the subgrid contributions are added to the resolved part of the Reynolds stress and the results are also plotted in figure 15(*b*). With respect to self-similarity figure 15(*a*) and 15(*b*) do not differ much.

Self-similarity in itself may not be sufficient evidence that a physically realistic flow is simulated. For that reason we compare the centre value of the turbulent kinetic energy $\frac{1}{2}R_{qq}$ (figure 14*a*) with the (untripped) experimental data from Bell & Mehta (1990, figure 4*a–c*). The experimental value in the self-similar region, 0.035, corresponds to $0.035(\Delta U)^2 = 0.14$ in our scales. It was somewhat higher ($0.043(\Delta U)^2 = 0.17$) just before self-similarity was achieved. The simulation results with the three dynamic models M4–6 are in reasonable agreement with these experimental observations. If we assume that the subgrid contributions increase the curves in figure 14(*a*) about 10% (see figure 15*b*), the M4 simulation slightly over-predicts and M5–6 slightly

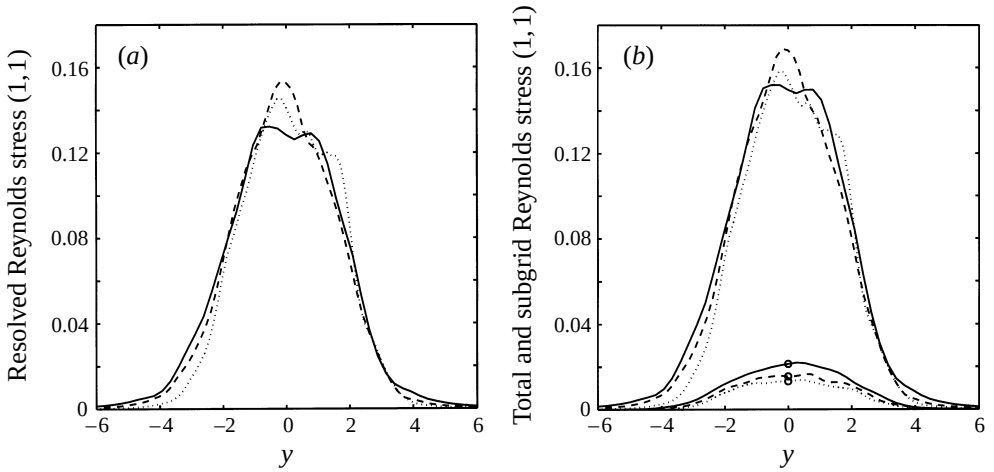

FIGURE 15. Profiles of Reynolds stress R_{11} versus $y = x_2/\delta(t)$ at $t = 120$ (solid), $t = 160$ (dashed) and $t = 200$ (dotted). (*a*) Resolved Reynolds stress R_{11}; (*b*) estimated subgrid part (symbol ○) and corrected R_{11} (no symbol).

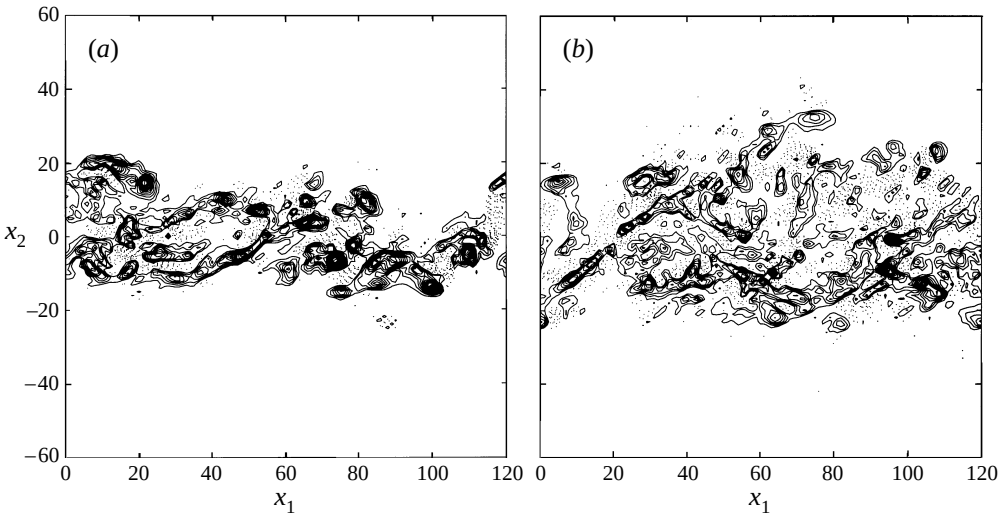

FIGURE 16. Positive (dotted) and negative (solid) contours of spanwise vorticity in the plane $x_3 = 90$ at $t = 160$ (*a*) and $t = 240$ (*b*). The contour increment equals 0.05.

under-predict the experimental result. Exact agreement with experimental statistics is not required, because, as remarked above, the specific self-similar state is probably not unique.

Finally, the spanwise vorticity in a planar cut of the domain at two distinct times in the M4 simulation is shown in figure 16. The large-scale roller structures in this simulation starting from uniform noise appear to be less prominent than in the simulations starting from an eigenfunction perturbation (see also Rogers & Moser 1994).

5. Conclusions

In this paper we have presented *a posteriori* tests of LES of the temporal mixing layer using six subgrid models: Smagorinsky (M1), similarity (M2), gradient (M3), dynamic eddy viscosity (M4), dynamic mixed (M5) and dynamic Clark (M6). The first three subgrid models form the basis for the latter three dynamic models. Two sets of simulations have been performed, at low and high Reynolds number respectively. The LES in the first set have been compared with DNS data, whereas in the analysis of the second set of simulations we focused on other aspects, such as self-similarity. The conclusions drawn from the first set of simulations are presented first.

In the first set of simulations the quality of a model is determined by the discrepancy of its results with the filtered DNS results. Furthermore, in order to determine whether the inclusion of the subgrid model is useful, comparisons with a coarse-grid simulation without any subgrid model (M0) have been performed. A summary of the results is found in table 2. When the models are arranged with respect to the overall accuracy of their results, the following sequence is obtained: M5, M6, M4, M2, M3, M1. The results of the latter two models are in general worse than the M0 results; incorporation of these subgrid-models in LES of the mixing layer is not useful. The other models in general give better results than M0. The overall results indicate that the dynamic mixed model displayed the best performance when compared to filtered DNS results. The dynamic mixed model was also observed to yield the most accurate results in comparative tests of subgrid models in LES of a driven cavity (Zang *et al.* 1993) and a rotating boundary layer (Wu & Squires 1995).

The Smagorinsky model was found to be excessively dissipative in the transitional regime. Comparison with the filtered DNS demonstrated that M1 strongly influences the linear evolution of disturbances, since the four-roller structure is not reproduced. Furthermore, M1 hindered the transition to turbulence. No positive spanwise vorticity was generated, the sudden growth of the momentum thickness did not occur and turbulent intensities and Reynolds stress profiles were under-predicted.

Although from the *a priori* point of view M2 and M3 are very similar and both provide highly accurate representations of the turbulent stress tensor (Vreman *et al.* 1995) they behave very differently in actual simulations: M2 yields reasonable results, whereas M3 leads to instabilities if no limiter is used. However, even with the incorporation of a limiter, M3 produces too many small scales and leads to inaccurate results for integral quantities and e.g. the streamwise turbulent intensity. In order to stabilize the gradient model, the inclusion of a dynamic eddy viscosity as in M6 is preferred over a limiter (M3), since the first case leads to more accurate results.

Examination of the energy spectra demonstrates that only the models which contain a dynamic eddy viscosity (M4–6) provide the correct amount of small scales. Due to insufficient dissipation of small scales by the subgrid model, the flow simulated with M0, M2 and M3 contains too many small structures. This gives rise to a higher molecular dissipation, which supplements the insufficient small-scale dissipation of the model. Although the dissipation for small scales is insufficient, the total energy dissipation provided by M2 was observed to be reasonable, since too much energy was subtracted from the large scales. It is remarkable that the dynamic eddy-viscosity model M4 provides satisfactory results, although it severely under-predicts the magnitude of the individual turbulent stress components. An adequate dissipative behaviour appears to be more important than a good prediction of the individual turbulent stresses. A suitable mechanism for this dissipation is provided by the similarity assumption used in the dynamic approach.

The models M2 and M5–6 have mechanisms to mimic the backscatter of energy from subgrid scales to resolved scales, but do not accurately predict it. However, actual LES of the mixing layer seems to require only a small amount of backscatter. The same is observed from the filtered DNS results, in which the backscatter is about 10% of the subgrid dissipation. Hence, a poor representation of the backscatter by the subgrid models is not too much of a problem.

In this paper we have presented *a posteriori* tests. In *a priori* tests the six models correlate with the real turbulent stress as follows: the correlation is high for M2 and M3, somewhat lower for M5 and M6 and very low for the eddy-viscosity models M1 and M4 (e.g. Liu *et al.* 1994*a*; Vreman *et al.* 1995). Meneveau (1994) remarks that *a priori* testing is often too pessimistic, i.e. a low correlation does not necessarily lead to poor results, which is confirmed by our results obtained with M4. However, *a priori* testing can also be much too optimistic, since a high correlation does not necessarily lead to good results as our results for M2 and M3 show.

The second set of LES with M0–6 concern a mixing layer at a much higher Reynolds number in a larger computational domain (§4). No DNS results are available to compare with, since the Reynolds number is too high to accurately resolve all scales with the present supercomputers.

Since the amount of subgrid dissipation obviously depends on the value of the Smagorinsky constant C_S, the dissipative behaviour of the Smagorinsky model could be better using a lower value for C_S. Therefore, in this case we also used the lower $C_S = 0.10$ in the simulation with M1. The model was still too dissipative in the laminar regime; the transition occurred, but too late, and in the turbulent regime the model was not sufficiently dissipative. Hence, a varying model coefficient that attains the appropriate value in transitional and turbulent regimes is required. The dynamic models meet this requirement.

The simulations with M0, M2 and M3 become unstable in the turbulent regime. M0 has no subgrid dissipation and the dissipation of M2 and M3 is insufficient to prevent an excessive amount of small scales.

The three dynamic models M4–6 adequately suppress the generation of small scales, but there are differences between the results of the three simulations. Within this group of models the dynamic eddy-viscosity model yields the most self-similar turbulent statistics.

Despite the large improvements originating from the dynamic approach, the results presented in this paper still show considerable discrepancies in several flow quantities, such as the profiles of the turbulent intensities and the momentum thickness. Additional improvement of subgrid modelling may be guided by the present results.

The results in this paper apply to the mixing layer at low Mach number. Details of the comparison may be valid only for this case, but the global features are expected to be more generally applicable. Examples of such global features are: the excessive dissipation of the Smagorinsky model, the insufficient dissipation of small scales by the similarity and gradient models, the relatively adequate subgrid-dissipation by the dynamic models and the under-predicted magnitude of the individual turbulent stress components by the dynamic eddy-viscosity model. In order to substantiate this, we are at present studying more complex flows, which are physically realizable and admit a quantitative comparison with experimental results. Examples of such flows are the spatial mixing layer and (separated) boundary layer flow. Also, the formulation of the LES approach to transonic compressible flows is subject of study.

The time for the computations was provided by the Stichting Nationale Computerfaciliteiten (National Computing Facilities Foundation, NCF), which is financially supported by the Nederlandse Organisatie van Wetenschappelijk Onderzoek (Netherlands Organization for Scientific Research, NWO). The authors thank the referees for their comments.

Appendix

The dynamic procedure requires formulations of the subgrid model at the F-level and the FG-level. The F-level is associated with the filter width Δ, the G-level with the filter width 2Δ and the FG-level with the filter width $\kappa\Delta$. The value of κ equals 2 for the spectral cut-off filter (Germano *et al.* 1991) and $\sqrt{5}$ for Gaussian filters (Germano 1992). For spectral cut-off and Gaussian filters, κ can be determined exactly, since the consecutive application of two of these filters yields a filter function of the same type. However, the consecutive application of two top-hat filters does not yield a top-hat filter and the value of κ should not be 2 (as used for instance by Zang *et al.* 1993). In this Appendix we argue that in conjunction with top-hat filters the optimum value of κ equals $\sqrt{5}$.

We denote the original filter function by G_a with filter width $a = \Delta$ and the test-filter function by G_b with filter width $b > a$. The filter function corresponding to the consecutive application of these two filters is denoted by H and satisfies the following formula:

$$H(\boldsymbol{y}) = \int_{\Omega} G_b(\boldsymbol{y} - \boldsymbol{z}) G_a(\boldsymbol{z}) \mathrm{d}\boldsymbol{z}. \tag{A 1}$$

If G_a and G_b are spectral filters, H is a spectral filter as well with filter width b, whereas if G_a and G_b are Gaussian filters, H is a Gaussian filter with filter width $(a^2 + b^2)^{1/2}$. However, the consecutive application of two top-hat filters is not a top-hat filter; the filter function H has a trapezoidal shape. In LES employing the dynamical procedure with top-hat filters, the filter width of H is usually assumed to be the same as the filter width of G_b (Zang *et al.* 1993). However, this approximation cannot be correct, because the H-filter will certainly render smoother signals than the G_b-filter, so the filter width associated with H should be larger than b. We proceed to show how an appropriate value for the filter width of H can be found. Since the three-dimensional filter function is usually a product of three one-dimensional filter functions, the analysis can be performed in one dimension. Suppose that H is the trapezoidal filter function resulting from the consecutive application of two one-dimensional top-hat filter functions G_a and G_b with $b > a$. This yields the following expression:

$$H(y) = \begin{cases} (1/ab)(y + \frac{1}{2}(b+a)) & \text{if } -\frac{1}{2}(b+a) < y < -\frac{1}{2}(b-a), \\ (1/b) & \text{if } -\frac{1}{2}(b-a) \leqslant y \leqslant \frac{1}{2}(b-a), \\ -(1/ab)(y - \frac{1}{2}(b+a)) & \text{if } \frac{1}{2}(b-a) < y < \frac{1}{2}(b+a), \\ 0 & \text{if } |y| \geqslant \frac{1}{2}(b+a)\ . \end{cases} \tag{A 2}$$

We next find an optimal approximation of H by a top-hat filter function G_c, given by

$$G_c(y) = \begin{cases} 1/c & \text{if } -\frac{1}{2}c < y < \frac{1}{2}c, \\ 0 & \text{if } |y| \geqslant \frac{1}{2}c\ . \end{cases} \tag{A 3}$$

For this purpose we minimize the L_2-norm of the error, which is a function of c:

$$\delta(c) = \|G_c - H\|. \tag{A 4}$$

The choice of the L_2-norm has the advantage that the error is also minimum in spectral space, due to Parseval's theorem. The minimum value of c will certainly satisfy $b - a \leqslant c \leqslant b + a$. In this range the square of the error equals (after some calculation)

$$(\delta(c))^2 = \frac{1}{b} - \frac{a}{3b^2} + \frac{b+a}{ab} + \frac{1}{c}\left(\frac{a}{2b} + \frac{b}{2a}\right) + \frac{c}{2ab}. \tag{A 5}$$

Minimisation of the error requires

$$\frac{\mathrm{d}}{\mathrm{d}c}(\delta(c))^2 = 0, \tag{A 6}$$

which finally yields

$$c = (a^2 + b^2)^{1/2}. \tag{A 7}$$

It is remarkable that this relation, which represents an optimal approximation for top-hat filters, is identical to the exact relation for Gaussian filters. Furthermore it appears that when equation (A 7) is satisfied for top-hat filters, not only is $\delta(c)$ minimum, but also the second moments of G_c and H are equal:

$$\int_{c/2}^{c/2} y^2 G_c(y)\mathrm{d}y = \int_{-(b+a)/2}^{(b+a)/2} y^2 H(y)\mathrm{d}y. \tag{A 8}$$

Usually the ratio between the filter width of the test and the original filter is equal to 2 ($b = 2a$), in which case equation (A 7) gives $c = \sqrt{5}a$, which corresponds to $\kappa = \sqrt{5}$.

REFERENCES

Bardina, J., Ferziger, J. H. & Reynolds, W. C. 1984 Improved turbulence models based on LES of homogeneous incompressible turbulent flows. *Rep. TF-19*. Department of Mechanical Engineering, Stanford.

Bell, J. H. & Mehta, R. D. 1990 Development of a two-stream mixing layer from tripped and untripped boundary layers. *AIAA J.* **28**, 2034–2042.

Blaisdell, G. A., Mansour, N. N. & Reynolds, W. C. 1993 Compressibility effects on the growth and structure of homogeneous turbulent shear flow. *J. Fluid Mech.* **256**, 443–485.

Brown, G. L. & Roshko, A. 1974 On density effects and large structure in turbulent mixing layers. *J. Fluid Mech.* **64**, 775–816.

Campagne, F. H., Pao, Y. H. & Wygnanski, I. J. 1976 On the two dimensional mixing region. *J. Fluid Mech.* **74**, 209–250.

Carati, D., Ghosal, S. & Moin, P. 1995 On the representation of backscatter in dynamic localization models. *Phys. Fluids* **7**, 606–616.

Carati, D. & Vanden Eijnden, E. 1996 On the self-similarity assumption in dynamic models for large eddy simulations. *Phys. Fluids* (submitted).

Clark, R. A., Ferziger, J. H. & Reynolds, W. C. 1979 Evaluation of subgrid-scale models using an accurately simulated turbulent flow. *J. Fluid Mech.* **91**, 1–16.

Comte, P., Lesieur, M. & Lamballais, E. 1992 Large and small-scale stirring of vorticity and a passive scalar in a 3D temporal mixing layer. *Phys. Fluids* A **4**, 2761.

Deardorff, J. W. 1970 A numerical study of three-dimensional turbulent channel flow at large Reynolds numbers. *J. Fluid Mech.* **41**, 453–480.

Deardorff, J. W. 1971 On the magnitude of the subgrid scale eddy viscosity coefficient. *J. Comput. Phys.* **7**, 120–133.

Dimotakis, P. E. & Brown, G. L. 1976 The mixing layer at high Reynolds number: large-structure dynamics and entrainment. *J. Fluid Mech.* **78**, 535–560.

Favre, A. 1983 Turbulence: space-time statistical properties and behavior in supersonic flows. *Phys. Fluids* **26**, 2851–2863.

Germano, M., Piomelli, U., Moin, P. & Cabot, W. H. 1991 A dynamic subgrid-scale eddy viscosity model. *Phys. Fluids* A **3**, 1760–1765.

Germano, M. 1992 Turbulence: the filtering approach. *J. Fluid Mech.* **238**, 325–336.

Germano, M. 1996 A statistical formulation of the dynamic model. *Phys. Fluids* **8**, 565–571.

Ghosal, S., Lund, T. S., Moin, P. & Akselvoll, K. 1995 A dynamic localization model for large-eddy simulation of turbulent flows. *J. Fluid Mech.* **286**, 229–255.

Gresho, P. 1991 Incompressible fluid dynamics: some fundamental formulation issues. *Ann. Rev. Fluid Mech.* **23**, 343–370.

Horiuti, K. 1995 Backward cascade of subgrid-scale kinetic energy in wall bounded and free turbulent flows. In *Proc. Turbulent Shear Flows 10, The Pennsylvania State University*, pp. 20.13-18.

Jiménez-Härtel, C. J. 1994 Analyse und Modellierung der Feinstruktur im wandnahen Bereich turbulenter Scherströmungen. *Forschungsbericht* 94-22. Institut für Strömungs- mechanik, Göttingen.

Kwak, D., Reynolds, W. C. & Ferziger, J. H. 1975 Three-dimensional time dependent computation of turbulent flow. *Report* TF-5. Stanford University.

Lilly, D. K. 1967 The representation of small-scale turbulence in numerical simulation experiments. In *Proc. IBM Scientific Computing Symp. on Environmental Sciences.* IBM Form no. 320-1951, 195-210.

Lilly, D. K. 1992 A proposed modification of the Germano subgrid-scale closure method. *Phys. Fluids* A **4**, 633–635.

Liu, S., Meneveau, C. & Katz, J. 1994*a* On the properties of similarity subgrid-scale models as deduced from measurements in a turbulent jet. *J. Fluid Mech.* **275**, 83–119.

Liu, S., Meneveau, C. & Katz, J. 1994*b* Experimental study of similarity subgrid-scale models of turbulence in the far-field of a jet. In *Direct and Large-Eddy Simulation I*, pp. 37–48. Kluwer.

Lund, T. S., Kaltenbach, H. J. & Akselvoll, K. 1995 On the behavior of centered finite difference schemes for large eddy simulation. In *Proc. Sixth Intl Symp. on Computational Fluid Dynamics. Lake Tahoe, NV, 4–8 September 1995.*

Luo, K. H. & Sandham, N. D. 1994 On the formation of small scales in a compressible mixing layer. In *Direct and Large-Eddy Simulation I*, pp. 335–346. Kluwer.

Meneveau, C. 1994 Statistics of turbulence subgrid-scale stresses: Necessary conditions and experimental tests. *Phys. Fluids* **6**, 815–833.

Moin, P. & Jimenez, J. 1993 Large Eddy Simulation of complex turbulent flows. *AIAA 24th Fluid Dyn. Conf. Orlando.*

Moin, P. & Kim, P. 1982 Numerical investigation of turbulent channel flow. *J. Fluid Mech.* **118**, 341–377.

Moser, R. D. & Rogers, M. 1993 The three-dimensional evolution of a plane mixing layer: pairing and transition to turbulence. *J. Fluid Mech.* **247**, 275–320.

Piomelli, U., Moin, P. & Ferziger, J. H. 1988 Model consistency in large eddy simulation of turbulent channel flows. *Phys. Fluids* **31**, 1884–1891.

Piomelli, U., Zang, T. A., Speziale, C. G. & Hussaini, M. Y. 1990*a* On the large-eddy simulation of transitional wall-bounded flows. *Phys. Fluids* A, **2**, 257–265.

Piomelli, U., Cabot, W. H., Moin, P. & Lee, S. 1990*b* Subgrid-scale backscatter in transitional and turbulent flows. *CTR Proc. Summer Program 1990*, pp. 19–30.

Piomelli, U. & Liu, J. 1994 Large-Eddy Simulation of rotating channel flows using a localized dynamic model. *Application of Direct and Large Eddy Simulation to Transition and Turbulence, AGARD Conf. Proc.* 551, pp. 3.1–9.

Ragab, S. A. & Wu, J. L. 1989 Linear instabilities in two-dimensional compressible mixing layers. *Phys. Fluids* A, **1**, 957–966.

Rogallo, R. S. & Moin, P. 1984 Numerical simulation of turbulent flows. *Ann. Rev. Fluid Mech.* **16**, 99–137.

Rogers, M. M. & Moser, R. D. 1994 Direct simulation of a self-similar turbulent mixing layer. *Phys. Fluids* **6**, 903–924.

Sandham, N. D. & Reynolds, W. C. 1991 Three-dimensional simulations of large eddies in the compressible mixing layer. *J. Fluid Mech.* **224**, 133–158.

Schumann, U. 1991 Direct and large eddy simulation of turbulence - summary of the state-of-the-

art 1991. Lecture Series 1991–02: *Introduction to the Modeling of Turbulence*. Von Karman Institute, Brussels.

Smagorinsky, J. 1963. General circulation experiments with the primitive equations. *Mon. Weather Rev.* **91**, 99–164.

Vreman, A. W. 1995. Direct and Large-Eddy Simulation of the compressible turbulent mixing layer. PhD Dissertation, University of Twente.

Vreman, B., Geurts, B. & Kuerten, H. 1994*a* Realizability conditions for the turbulent stress tensor in large eddy simulation. *J. Fluid Mech.* **278**, 351–362.

Vreman, B., Geurts, B. & Kuerten, H. 1994*b* On the formulation of the dynamic mixed subgrid-scale model. *Phys. Fluids* **6**, 4057–4059.

Vreman, B., Geurts, B. & Kuerten, H. 1995 A priori tests of Large Eddy Simulation of the compressible plane mixing layer. *J. Engng Maths* **29**, 299–327.

Vreman, B., Geurts, B. & Kuerten, H. 1996*a* Comparison of numerical schemes in Large Eddy Simulation of the temporal mixing layer. *Intl J. Numer. Meth. Fluids* **22**, 297–311.

Vreman, B., Geurts, B. & Kuerten, H. 1996*b* Large eddy simulation of the temporal mixing layer using the Clark model. *Theor. Comput. Fluid Dyn.* **8**, 309–324.

Vreman, A. W., Sandham, N. D. & Luo, K. H. 1996*c* Compressible mixing layer growth rate and turbulence characteristics. *J. Fluid Mech.* **320**, 235–258.

Wu, X., & Squires, K. D. 1995 Large-eddy simulation of a canonical three-dimensional boundary layer. In *Proc. Turbulent Shear Flows 10, The Pennsylvania State University*, pp. 8.19-24.

Zang, Y., Street, R. L. & Koseff, J. R. 1993 A dynamic mixed subgrid-scale model and its application to turbulent recirculating flows. *Phys. Fluids* A **5**, 3186–3196.